The Inositol Trisphosphate Receptor (IP_3R) is Dispensable for Rotavirus-induced Ca^{2+} Signaling and Replication but Critical for Paracrine Ca^{2+} Signals that Prime Uninfected Cells for Rapid Virus Spread

Jacob L. Perry, Francesca J. Scribano, John T. Gebert, Kristen A. Engevik, Jenna M. Ellis, and Joseph M. Hyser

Alkek Center for Metagenomic and Microbiome Research; Department of Molecular Virology and Microbiology, Houston, TX, USA.

Running title: Ca^{2+} waves prime nearby cells for rotavirus spread

*Correspondence should be sent to:

Joseph M. Hyser

Joseph.Hyser@bcm.edu

No conflicts of interest exist.

Abstract.

Rotavirus is a leading cause of viral gastroenteritis. A hallmark of rotavirus infection is an increase in cytosolic Ca^{2+} caused by the nonstructural protein 4 (NSP4). NSP4 is a viral ion channel that releases Ca^{2+} from the endoplasmic reticulum (ER) and the increase in Ca^{2+} signaling is critical for rotavirus replication. In addition to NSP4 itself, host inositol 1,4,5-trisphosphate receptor (IP_3R) ER Ca^{2+} channels may contribute to rotavirus-induced Ca^{2+} signaling and by extension, virus replication. Thus, we set out to determine the role of IP_3R Ca^{2+} signaling during rotavirus infection using IP_3R-knockout MA104-GCaMP6s cells (MA104-GCaMP6s-IP_3R-KO), generated by CRISPR/Cas9 genome editing. Live Ca^{2+} imaging showed that IP_3R-KO did not reduce Ca^{2+} signaling in infected cells but eliminated rotavirus-induced intercellular Ca^{2+} waves (ICWs) and therefore the increased Ca^{2+} signaling in surrounding, uninfected cells. Further, MA104-GCaMP6s-IP_3R-TKO cells showed similar rotavirus susceptibility, single-cycle replication, and viral protein expression as parental MA104-GCaMP6s cells. However, MA104-GCaMP6s-IP_3R-TKO cells exhibited significantly smaller rotavirus plaques, decreased multi-round replication kinetics, and delayed virus spread, suggesting that rotavirus-induced ICW Ca^{2+} signaling stimulates virus replication and spread. Inhibition of ICWs by blocking the P2Y1 receptor also resulted in decreased rotavirus plaque size. Conversely, exogenous expression of P2Y1 in LLC-MK2-GCaMP6s cells, which natively lack P2Y1 and rotavirus ICWs, rescued the generation of rotavirus-induced ICWs and enabled plaque formation. In conclusion, this study shows that NSP4 Ca^{2+} signals fully support rotavirus replication in individual cells; however, IP_3R is critical for rotavirus-induced ICWs and virus spread by priming Ca^{2+}-dependent pathways in surrounding cells.

39 **Importance.**

40 Many viruses exploit host Ca^{2+} signaling to facilitate their replication; however, little is known
41 about how distinct types of Ca^{2+} signals contribute to the overall dysregulation of Ca^{2+} signaling
42 or promote virus replication. Using cells lacking IP_3R, a host ER Ca^{2+} channel, we could
43 differentiate between intracellular Ca^{2+} signals within virus-infected cells and intercellular Ca^{2+}
44 waves (ICWs), which increase Ca^{2+} signaling in neighboring, uninfected cells. In infected cells,
45 IP_3R was dispensable for rotavirus-induced Ca^{2+} signaling and replication, suggesting the
46 rotavirus NSP4 viroporin supplies these signals. However, IP_3R-mediated ICWs increase
47 rotavirus replication kinetics and spread, indicating that the Ca^{2+} signals from the ICWs may
48 prime nearby uninfected cells to better support virus replication upon eventual infection. This
49 “pre-emptive priming” of uninfected cells by exploiting host intercellular pathways in the vicinity
50 of virus-infected cells represents a novel mechanism for viral reprogramming of the host to gain
51 a replication advantage.

52

53 **Introduction.**

54 Calcium (Ca^{2+}) signaling is a cornerstone of cellular communication and is critical for
55 maintaining homeostasis and responding to damage or infection(1). As such, it is unsurprising
56 that many viruses have evolved strategies to exploit these pathways to facilitate virus replication
57 and spread (2). However, the highly interconnected nature of Ca^{2+} signaling has made it
58 challenging to understand how viral and host proteins interact to orchestrate the patterns of Ca^{2+}
59 dysregulation that are observed during infection. One key strategy for virus-induced calcium
60 dysregulation is the expression of viral ion channels, or viroporins, which can conduct Ca^{2+}
61 across host cell membranes (3). The rotavirus nonstructural protein 4 (NSP4) is among the most
62 well-characterized Ca^{2+} conducting viroporins and rotavirus has become a leading model system
63 to study how viruses exploit Ca^{2+} signaling to promote their replication (4). Yet, the interplay
64 between rotavirus- and host-induced Ca^{2+} signaling pathways remain incompletely
65 characterized.

66 Numerous studies show that NSP4 elevates cytosolic Ca^{2+} levels during infection (5-7).
67 NSP4 is a multifunctional endoplasmic reticulum (ER), transmembrane glycoprotein (8, 9) that
68 increases the Ca^{2+} permeability of the ER by forming a Ca^{2+} permeable viral ion channel
69 (viroporin) (10, 11). The NSP4-mediated release of ER Ca^{2+} in turn activates a host process
70 known as store-operated calcium entry (SOCE) to further elevate cytosolic Ca^{2+} levels (12). This
71 is critical for multiple steps in rotavirus replication, including the activation of the autophagy
72 pathway and assembly of the rotavirus outer capsid protein, VP7 (12, 13). Yet, NSP4 may play
73 both a direct and an indirect role in ER Ca^{2+} release, through interaction with host channels. The
74 two main eukaryotic ER Ca^{2+} release channels are the ryanodine receptor (RyR) and the inositol-
75 1,4,5-trisphosphate receptor (IP_3R), and while RyR expression is generally restricted to excitable
76 cells, IP_3R is widely expressed in most cell types (14). Mammals have three IP_3R genes, each
77 with multiple splice variants that provides nuance to the regulation of IP_3R Ca^{2+} release and

78 therefore the ability to shape Ca^{2+} signals (14, 15). The IP_3R channel is activated by IP3 and
79 channel opening is regulated by cytosolic Ca^{2+} in a biphasic manner, such that low cytosolic
80 Ca^{2+} levels potentiates ER Ca^{2+} release and increasing cytosolic Ca^{2+} levels inhibit ER Ca^{2+}
81 release (16). Thus, even though the NSP4 viroporin directly alters ER and cytosolic Ca^{2+}, NSP4
82 Ca^{2+} release may also potentiate IP_3R activity, increasing the Ca^{2+} dysregulation of host cells.

83 In addition to NSP4 and IP_3R crosstalk within infected cells, we recently discovered that
84 rotavirus infection triggers intercellular Ca^{2+} waves (ICWs) through the release of ADP from
85 infected cells and activation of P2Y1 purinergic receptors on neighboring cells. Activation of
86 P2Y1 receptors results in an IP_3R-mediated ER Ca^{2+} signal and since many ICWs are produced
87 during infection, this significantly increases Ca^{2+} signaling in neighboring, uninfected cells as
88 well (17). Thus, the ER Ca^{2+} store is a critical source of Ca^{2+} signals in both rotavirus infected
89 and the nearby uninfected cells and IP_3R has the potential to significantly impact the overall
90 landscape of rotavirus induced Ca^{2+} signaling dysregulation.

91 Thus, the goal of this study is to examine the contribution of IP_3R to rotavirus Ca^{2+}
92 dysregulation and by extension, its role in rotavirus infection, replication and spread. While
93 HEK293 and HeLa cells with genetic knockout of all three IP_3R genes (e.g., IP_3R1, IP_3R2, and
94 IP_3R3) have been established previously, these cell lines are suboptimal for studying rotavirus
95 replication and it is not known whether they support the rotavirus ICW signaling pathway (15,
96 18). Thus, we generated an IP_3R triple knockout in MA104 cells, a vervet monkey (*Chlorocebus*
97 *pygerythrus*) kidney cell line commonly used to study rotavirus (17, 19, 20). We found that IP_3R
98 was not necessary for aberrant Ca^{2+} signaling in infected cells, but was necessary for Ca^{2+}
99 dysregulation in neighboring, uninfected cells. In parallel, IP_3R was dispensable for single-round
100 rotavirus infection and replication, but lack of IP_3R, and therefore lack of ICW signaling, strongly
101 reduced rotavirus spread. This study provides new insights into mechanisms exploited by

102 viruses to reprogram infected cells but also to pre-program surrounding cells for subsequent
103 rounds of infection.
104

105 **Materials and Methods.**

106 **Cells and viruses.**

107 All cells were cultured in complete DMEM [high glucose DMEM supplemented with 10% fetal
108 bovine serum (FBS) and Antibiotic/Antimycotic (Invitrogen)] and incubated at 37°C in 5% CO_2.
109 HEK293 and HEK293-IP_3R-TKO cells were provided by Dr. David Yule (15, 21). The MA104
110 (vervet monkey kidney), LLC-MK2 (rhesus monkey kidney), HEK293 and HEK293-IP_3R-TKO
111 cell lines were engineered to express the cytosolic Ca^{2+} sensor, GCaMP6s, as previously
112 described (20, 22). All rotavirus infections were at the indicated MOI for 1 hr with a recombinant
113 SA11 expressing mRuby3 from gene 7 (SA11-mRuby), which was propagated as previously
114 described (20, 23).

115 **MA104-GCaMP6s-**IP_3R **triple-knockout generation.**

116 *CRISPR/Cas9 development and transduction*

117 MA104 cells lacking IP_3R expression (MA104-GCaMP6s-IP_3R-TKO) were generated by
118 lentivirus transduction to introduce Cas9 and small guide RNAs (gRNAs) to IP_3R1, IP_3R2, and
119 IP_3R3 (Table 1). The lentivirus construct was designed by our lab and manufactured by
120 VectorBuilder (Chicago, IL). MA104-GCaMP6s cells were transduced with MOI 10 in complete
121 DMEM supplemented with 10 µg/mL polybrene (21). At 72 hours post-transduction, cells were
122 passaged in the presence of 40 µg/mL blasticidin. After 2 weeks of selection, cells were dilution
123 cloned and resulting clones were screened for lack agonist-induced IP_3R Ca^{2+} responses, as
124 described below.

125 *Sequencing of* IP_3R *triple-knockout*

126 Genomic DNA was extracted using a PureLink™ gDNA mini kit (Invitrogen, USA). PCR
127 amplification was performed using KOD Hotstart polymerase kit (EMD Millipore) and primers
128 flanking the gRNA target sites (Table 2). PCR products were cloned in TOPO-TA vectors

129 (Invitrogen, USA) and a minimum of six bacterial colonies for each IP_3R gene were sequenced
130 using M13 forward and reverse primers (Azenta, NJ, USA). To determine the distribution of
131 mutant alleles, sequences were mapped to the genomic DNA using SnapGene.
132
133 **LLC-MK2-GCaMP6s P2Y1 knock-in generation.**
134 LLC-MK2-GCaMP6s P2Y1 knock in lines were generated by lentiviral transduction of the human
135 P2RY1 receptor. The P2Y1 cDNA clone was purchased from GenScript (Piscataway, NJ, USA)
136 and subcloned into pLVX-IRES-Neo lentivirus vector (Takara Bio) and packaged by the BCM
137 Vector Development Core. LLC-MK2-GCaMP6s cells were transduced with MOI 10 in 10 μg/mL
138 polybrene and at 72 hr post-transduction selected using 500 μg/mL G418. (21). Presence of
139 functional P2Y1 was verified by Ca^{2+} imaging for a Ca^{2+} response to 25 nM ADP.
140
141 **Ca^{2+} agonist treatment.**
142 MA104-GCaMP6s and MA104-GCaMP6s-IP_3R-TKO monolayers were placed in Ca^{2+} free
143 Hank's Balanced Salt Solution (HBSS, Invitrogen) and incubated for ~1 hr to equilibrate. For
144 agonist testing, we used 50 μM ADP for purinergic receptors, 0.75 μM AC55541 or 2 μM
145 Worthington's trypsin for PAR2 receptors, or 1 μM thapsigargin to inhibit SERCA pumps. Cells
146 were first imaged for 30 seconds to establish a baseline. Following agonist stimulation with 50
147 μL of agonist solution, cells were imaged for 2 minutes to capture the peak Ca^{2+} response.
148 Imaging acquisition was 50 ms exposures with a 1 second interval.
149
150 **Live-cell Ca^{2+} imaging of virus infection.**
151 Cell monolayers were grown in Ibidi 8-well chamber slides. On the day of imaging, media was
152 replaced with FluoroBrite-Plus media [FluoroBrite DMEM supplemented with 1X nonessential

153 amino acids, 1X Glutamax, 1X sodium pyruvate, and 15 μM HEPES (Invitrogen)]. Rotavirus was
154 diluted in FluoroBrite-Plus and cells were mock- (FluoroBrite-Plus alone) or rotavirus-infected at
155 MOI 0.01. The inoculum was removed after 1 hr, fresh FluoroBrite-Plus was added, and the slide
156 was mounted into the microscope environmental chamber (37°C in 5% CO_2) to equilibrate.
157 Imaging was performed using a Nikon TiE inverted microscope using a SPECTRAX LED light
158 source (Lumencor) and either a 20x Plan Fluor (NA 0.45) or a 20X Plan Apo (NA 0.75), objective
159 as previously described (20). Nikon Elements Advanced Research v4.5 software was used for
160 data acquisition and image analysis. Fluorescence intensity values were exported to Microsoft
161 Excel and GraphPad Prism for data analyses.
162
163 **Viral infectivity assay.**
164 MA104-GCaMP6s and MA104-GCaMP6s-IP_3R-TKO monolayers grown in 96-well plates were
165 inoculated with 2-fold serial dilutions of SA11-mRuby. The inoculum was removed 1 hr post-
166 infection, then the cells were rinsed twice with PBS and cultured in FBS-free DMEM for ~16 hrs.
167 Monolayers were fixed in ice cold methanol for 20 minutes at 4°C, washed three times with PBS,
168 and immunostained for 2 hrs using a rabbit anti-rotavirus antisera (strain Alabama) at 1:1000 in
169 PBS, followed by incubation for 1 hr with goat anti-rabbit IgG:AlexaFluor555 at 1:1000 in PBS,
170 and quantitation by fluorescence microscopy.
171
172 **Single-cycle and multi-cycle rotavirus yield assay.**
173 MA104-GCaMP6s and MA104-GCaMP6s-IP_3R-TKO monolayers were inoculated with SA11-
174 mRuby for 1 hr. We used an MOI of 0.01 for single-cycle replication assays and 24 PFU/well for
175 multi-cycle replication assays. For single-cycle assays, cells were maintained in DMEM without
176 trypsin, which prevents rotavirus spread due to lack of VP4 spike protein cleavage and harvested
177 at 24 hpi. For multi-cycle assays, cells were maintained in DMEM with 1 µg/mL Worthington's

178 trypsin and harvested at 24-, 48-, 72-, and 96-hpi. Virus titration was performed by plaque assay
179 (see below).
180
181 **Plaque assay.**
182 Monolayers of MA104 or LLC-MK2 cells, or their modified derivatives, were inoculated with 10-
183 fold serial dilutions of virus samples in FBS-free DMEM. After the inoculum was removed, 3 mL
184 of overlay (1.2% Avicel in FBS-free DMEM supplemented with 0.1 mg/mL DEAE dextran and 1
185 μg/mL Worthington's trypsin) was added to each well and plates were incubated for 3-4 days.
186 After removing the overlay, plates were washed and stained with crystal violet or imaged by
187 fluorescence microscopy prior to crystal violet staining.
188
189 **Immunoblot analysis.**
190 Confluent MA104-GCaMP6s and MA104-GCaMP6s-IP_3R-TKO cells inoculated with SA11-
191 mRuby (MOI 10) and then harvested in RIPA buffer at 2, 4, 6, 8, and 10 hpi (20). Samples were
192 boiled for 10 minutes at 100°C in SDS-PAGE sample buffer and separated on Tris-glycine 4–
193 20% SDS-PAGE gels (BioRad) and blotted to nitrocellulose, which was blocked with 10% non-
194 fat dry milk in PBS (BLOTTO). Antibodies were diluted in 0.1% BLOTTO and were: rabbit anti-
195 rotavirus [strain Alabama, (1:1000)] (20), rabbit antisera to SA11 NSP4-aa120-146 (1:2000) (24),
196 and mouse anti-GAPDH (1:2000).
197
198 **Immunofluorescence.**
199 MA104 cell monolayers infected with SA11-mRuby (MOI 1) were fixed at 9 hpi, washed, and
200 incubated overnight at 4°C with rabbit antisera against NSP4 (anti-NSP4-aa114-135) and guinea
201 pig antisera against NSP5 (gift from Dr. Mary Estes at Baylor College of Medicine)(24, 25).
202 Monolayers were washed and incubated for 2 hours at room temperature with fluorescent-

203 conjugated secondary antibodies [anti-Rabbit DyLight 488; anti-guinea pig DyLight 549
204 (Rockland)] diluted 1:2000 in PBS. Monolayers were imaged using a 63X objective on a Zeiss
205 LSM980 confocal microscope with Airyscan. Mander's coefficients were determined by
206 calculating the ratio signal intensity for NSP4 colocalized with that of NSP5 to the overall intensity
207 of the NSP4 signal in a given image following background subtraction. Analyses used three
208 images per group for a total of 46 MA104 parental and 63 MA104-IP_3R-TKO cells.
209

210 **Detection of ADP release from cells.**

211 Confluent MA104-GCaMP6s and MA104-GCaMP6s-IP_3R-TKO cells were infected with SA11-
212 mRuby (MOI 10) and then maintained in 300 µL FluoroBrite-Plus with 20 µM ARL67156, an
213 ecto-ATPase inhibitor. At ~5 hpi, the supernatant was removed and used to treat parental
214 MA104-GCaMP6s cell monolayers to evoke a Ca^{2+} response, which was monitored by live
215 imaging of GCaMP6s fluorescence and quantitated by measuring the maximum increase in
216 GCaMP6s fluorescence after addition of the supernatant. Specificity of the Ca^{2+} response for
217 P2Y1 activation was determined by pretreating cells with 10 µM BPTU, a P2Y1-selective blocker.
218

219 **Quantitative PCR**

220 LLC-MK2-GCaMP6s and LLC-MK2-GCaMP6s+P2Y1 cells were grown to confluency in a 24-
221 well plate. Total RNA was extracted from cell monolayers using TRIzol (Ambion) according to
222 the manufacturer's instructions. 300 ng of RNA was used to generate cDNA with SensiFAST
223 synthesis reagents (Bioline). Quantitative PCR was performed with Fast SYBR green (Applied
224 Biosystems) with a QuantStudio 3 thermocycler. Purinergic receptor genes were normalized to
225 18s and expression relative to the lowest expressed gene (P2Y12) was calculated using the
226 $\Delta\Delta C_t$ method. Primer sequences have been published previously and can be found in Table 3
227 (26).

228

229 **SA11-mRuby detection in plaques.**

230 Rotavirus SA11-mRuby plaques were visualized by fluorescence microscopy using a Nikon TiE
231 inverted microscope as described above. Images were taken from a 6-well tissue culture plate
232 with a 10X Plan Fluor objective (NA 0.30). Whole-well images were obtained by taking a 15 mm
233 x 15 mm stitch with blending and 10% overlap.

234

235 **Statistical analyses.**

236 Statistics were completed using GraphPad Prism (version 8.4.3). Unless stated, all experiments
237 were performed in biological triplicate. The threshold for Ca^{2+} spikes is a 5% increase in GCaMP
238 fluorescence, as previously defined for this system (20). We performed column statistics to
239 determine the normality of the data sets. We used unpaired Student's t test for data sets with a
240 parametric distribution or a Mann-Whitney test for data sets with a nonparametric distribution.
241 We applied a one-way ANOVA with proper correction when applicable for comparing sample
242 groups to control groups. Differences were determined statistically significant if the P value was
243 <0.05. For all figures, P value notations are as follows: *P <0.05, **P <0.01, ***P <0.001, and
244 ****P <0.0001.

245 **Results.**

246 Previous studies have shown that rotavirus NSP4's viroporin function is a critical
247 mechanism for the dysregulation of cellular Ca^{2+} homeostasis during infection (7, 20). Yet, NSP4
248 crosstalk with host IP_3R channels could contribute to the overall Ca^{2+} signaling in infected cells
249 and the recently discovered intercellular Ca^{2+} waves (ICWs) induced by rotavirus are generated
250 by IP_3R Ca^{2+} release upon activation of P2Y1 receptors (14-17). Thus, we investigated the role
251 of IP_3R in the rotavirus-induced Ca^{2+} signaling landscape using IP_3R-null cell lines generated by
252 genomic editing. First, we obtained IP_3R triple-knockout (IP_3R-TKO) HEK293 cells, which
253 express no functional IP_3R isoforms, and tested whether rotavirus infection elevates Ca^{2+}
254 signaling similar to MA104 cells (15). Using long-term, time-lapse Ca^{2+} imaging, we found that
255 rotavirus infected MA104-GCaMP6s cells exhibited increased Ca^{2+} signaling, as we previously
256 described (20). Representative images show both the low amplitude intracellular Ca^{2+} signals
257 observed in rotavirus-infected cells (at 354 min and 360 min), as well as high amplitude ICWs
258 that propagate to surrounding uninfected cells (396 min) (Figure 1A, Movie 1). Representative
259 traces show mock-infected cells exhibit no strong Ca^{2+} signaling events (Figure 1B, black line),
260 but rotavirus-infected cells exhibited a strong increase in dynamic Ca^{2+} signaling (Figure 1B, red
261 line). Further, the intracellular Ca^{2+} signals, highlighted in the magenta bracket, occur before the
262 onset of ICWs (Figure 1B). This increase in Ca^{2+} signaling results in significantly more Ca^{2+}
263 spikes in rotavirus-infected than in mock infected cells (Figure 1C).

264 Next, to test the role of IP_3R in dysregulation of Ca^{2+} signaling during rotavirus infection,
265 we examined Ca^{2+} signaling in SA11-mRuby infected parental HEK293-GCaMP6s and HEK293-
266 GCaMP6s-IP_3R-TKO cells (Figure 1D-F). Representative images (Figure 1D) and Ca^{2+} signaling
267 traces (Figure 1E) show that both parental HEK293-GCaMP6s and HEK293-GCaMP6s-IP_3R-
268 TKO cells exhibit robust Ca^{2+} signaling during rotavirus infection (red lines) that is much greater
269 than in mock-infected cells (black lines). We observe numerous intracellular Ca^{2+} signals in both

270 cell lines but only a few, small ICWs in parental HEK293-GCaMP6s cells. There were no ICWs
271 in the HEK293-GCaMP6s-IP_3R-TKO cells because, as a Gq-coupled GPCR, P2Y1 evokes an
272 IP_3R-mediated release of ER Ca^{2+} (Figure 1D and Movie 2). Quantitation of Ca^{2+} signaling in
273 parental HEK293-GCaMP6s and HEK-293-GCaMP6s-IP_3R-TKO cells show both cell types had
274 a significant increase in overall spikes per cell compared to mock cells (Figure 1F). While we
275 observed a small, but statistically significant, increase in overall Ca^{2+} signaling in HEK293-
276 GCaMP6s-IP_3R-TKO cells compared to parental HEK293-GCaMP6s cells (Figure 1F), the
277 critical observation is that there was no *decrease* in rotavirus-induced Ca^{2+} signaling in HEK293-
278 GCaMP6s-IP_3R-TKO cells. Together, these data show rotavirus infection produces robust Ca^{2+}
279 signaling in both MA104 and HEK293 cells, and this is not decreased in the absence of IP_3R.
280 However, HEK293 cells are suboptimal for examining rotavirus-induced Ca^{2+} signaling, since
281 they do not exhibit robust ICWs and therefore do not have distinct intracellular and intercellular
282 signaling patterns. Thus, for further investigation into the role of IP_3R-mediated signaling during
283 rotavirus infection, we aimed to establish an MA104-GCaMP6s-IP_3R-TKO cell line.

284 **Generation MA104-GCaMP6s cells lacking IP_3R expression.**

285 To generate an MA104-GCaMP6s cell line lacking IP_3R expression, we generated a
286 CRISPR-Cas9 lentivirus construct that expresses individual gRNAs targeted to each IP_3R gene
287 (Table 1). Our workflow to generate MA104-GCaMP6s-IP_3R-TKO cells is depicted in Figure 2A.
288 For screening and validation, we used two different GPCR agonists to activate IP_3R-mediated
289 Ca^{2+} responses: 50 μM ADP to activate P2Y purinergic receptors and 0.75 μM AC55541 to
290 activate the Protease-activated Receptor 2 (PAR2). We identified 8 clones that exhibited little to
291 no response to these two agonists (Figure 2B) and chose clone F3 for full characterization, which
292 will be designated MA104-GCaMP6s-IP_3R-TKO cells for the remainder of this paper.

293 To functionally validate the loss of IP_3R Ca2+ signals in MA104-GCaMP6s-IP_3R-TKO
294 cells, we performed live imaging to measure Ca^{2+} responses to ADP and PAR2 agonist AC55541
295 (Figure 2C-D). For both agonists, MA104-GCaMP6s-IP_3R-TKO cells exhibit no increase in Ca^{2+}
296 and a small, but reproducible, decrease in GCaMP6s fluorescence (Figure 2C-D, red traces;
297 Movie 3). To validate these cells maintain an ER Ca^{2+} store, we treated cells with thapsigargin
298 to inhibit SERCA pumps. We found thapsigargin induced an increase in GCaMP6s fluorescence
299 for both parental and IP_3R-TKO cells, and peak signal from IP_3R-TKO cells was significantly
300 greater than that of parental MA104-GCaMP6s cells (Figure 2E). This indicates that IP_3R-TKO
301 cells have a higher ER Ca^{2+} load than that of parental MA104-GCaMP6s cells, which would be
302 expected in the absence of basal IP_3R activity. Finally, sequence analyses of MA104-GCaMP6s-
303 IP_3R-TKO cells identified the mutations at the gRNA sites for each IP_3R gene. To assess the
304 distribution of mutations, we amplified the gRNA sites for each gene, PCR-cloned amplicons,
305 and sequenced 6 plasmids for each IP_3R gene. We found a deletion mutation for IP_3R1, three
306 different insertion/deletion mutations for IP_3R2 and a single allele insertion for IP_3R3 (Figure 2F),
307 but no wild-type sequences were isolated, consistent with the lack of agonist-induced Ca^{2+}
308 responses from these cells. Together, these data show that we have successfully generated an
309 MA104-GCaMP6s cell line lacking IP_3R expression to better examine the role of IP_3R-mediated
310 ER Ca^{2+} release during rotavirus infection.

311 **Rotavirus-induced Ca^{2+} signaling in the absence of IP_3R.**

312 We previously found that rotavirus infection results in activation of highly dynamic Ca^{2+}
313 signaling throughout infection (20). Now by generating MA104-GCaMP6s-IP_3R-TKO cells, we
314 set out to determine how the lack of IP_3R affects rotavirus-induced Ca^{2+} signaling. We performed
315 long-term, time-lapse Ca^{2+} imaging of both parental MA104-GCaMP6s and MA104-GCaMP6s-
316 IP_3R-TKO cells infected with SA11-mRuby rotavirus, and representative images are shown in

317 Figure 3A. As previously characterized, rotavirus infected parental MA104-GCaMP6s cells
318 exhibit an increase in intracellular Ca^{2+} signals present, as well as production of intercellular
319 Ca^{2+} waves (ICWs) (Figure 3A, top; Movie 4). In MA104-GCaMP6s-IP_3R-TKO cells, we still
320 observed robust intracellular Ca^{2+} signaling in rotavirus-infected cells, but no ICWs were
321 produced (Figure 3A, bottom; Movie 4). Next, we compared Ca^{2+} signaling phenotypes between
322 parental MA104-GCaMP6s and MA104-GCaMP6s-IP_3R-TKO cells, with 4 representative traces
323 for each shown in Figure 3B. We found both cell types exhibit a very similar pattern of robust
324 Ca^{2+} signaling that progressively increases over the course of infection but mock-infected cells
325 exhibited only basal level signaling (Figure 3B). Further, though both cell lines show increased
326 Ca^{2+} signaling dynamics, there were fewer high amplitude Ca^{2+} signals in MA104-GCaMP6s-
327 IP_3R-TKO cells, which likely represents autocrine activation of P2Y1 during ICWs (Figure 3B,
328 arrows). Next, we quantitated the number of Ca^{2+} spikes in rotavirus-infected and uninfected
329 neighboring cells 3 and 5 cells away (NB3 and NB5, respectively) to capture ICWs (Figure 3C).
330 In parental MA104-GCaMP6s cells, we found a significant increase in Ca^{2+} signaling in both
331 infected and neighboring cells, consistent with our previous studies (20). In MA104-GCaMP6s-
332 IP_3R-TKO cells, there was a significant increase in Ca^{2+} signaling in rotavirus-infected cells but
333 no increase in the neighboring cells, consistent with the lack of ICWs (Figure 3C). Interestingly,
334 in rotavirus-infected MA104-GCaMP6s-IP_3R-TKO cells, we found no significant decrease in
335 overall Ca^{2+} signaling (Figure 3C). Since MA104-GCaMP6s-IP_3R-TKO cells did not produce
336 ICWs, we wanted to determine whether the cells were still releasing ADP during infection. To
337 test this, parental MA104-GCaMP6s and MA104-GCaMP6s-IP_3R-TKO cells were mock or
338 rotavirus-infected and incubated in the presence of ARL67156, an ecto-nucleotidase inhibitor,
339 to stabilize extracellular purines. At 5 hpi, a time point when ICWs have begun, media was
340 removed from mock and infected cells and added to parental MA104-GCaMP6s cells. We found
341 that media from rotavirus-infected cells induced a significantly greater Ca^{2+} response than that

342 from mock infected cells, and the Ca^{2+} response was blocked by the P2Y1 inhibitor BPTU (Figure
343 3D). Together, this indicated that the loss of IP_3R does not reduce the rotavirus-induced release
344 of ADP during infection and that the IP_3R-independent arms of the P2Y1 signaling pathway are
345 likely intact. These data in MA104 cells echo that of our initial studies in HEK293-GCaMP6s-
346 IP_3R-TKO cells, in that rotavirus still dramatically increases Ca^{2+} signaling within infected cells
347 in the absence of IP_3R (Figure 1E). Yet, loss of IP_3R resulted in the abrogation of rotavirus
348 induced ICWs and significantly reduced the increase in Ca^{2+} signaling in surrounding uninfected
349 cells, which ultimately changes the overall Ca^{2+} signaling landscape during infection.

350

351 **Role of IP_3R in rotavirus infection and replication.**

352 Numerous studies have confirmed that increased cytosolic Ca^{2+} is critical for rotavirus
353 replication (12, 13, 27). Thus, we next used parental MA104-GCaMP6s and MA104-GCaMP6s-
354 IP_3R-TKO cells to assess whether IP_3R signaling plays a role in rotavirus infectivity and/or
355 replication. First, we compared SA11-mRuby plaque phenotypes between parental MA104-
356 GCaMP6s and MA104-GCaMP6s-IP_3R-TKO cells, discovering a major difference in plaque
357 morphology (Figure 4A). MA104-GCaMP6s cell plaques fully cleared the monolayer and had
358 clean margins (Figure 4A, Top) in contrast to MA104-GCaMP6s-IP_3R-TKO cells, which exhibited
359 a similar number of plaques (i.e., no difference in measured titer); however, the plaques were
360 turbid with most of the monolayer remaining intact (Figure 4A, Bottom). Quantification of plaque
361 diameters showed rotavirus formed significantly smaller plaques on MA104-GCaMP6s-IP_3R-
362 TKO cells than on parental MA104-GCaMP6s cells (Figure 4A). Due to this substantial difference
363 in plaque formation, we next determined whether loss of IP_3R affected rotavirus infectivity or
364 single-cycle virus yield. We first determined infectivity of SA11-mRuby for both parental MA104-
365 GCaMP6s and MA104-GCaMP6s-IP_3R-TKO cells using a fluorescent focus assay (FFA) and

366 found no differences in the observed titer, indicating that rotavirus infects both cell lines with the
367 same efficiency (Figure 4B). This is consistent with both our live imaging studies (Figure 3) and
368 plaque assay (Figure 4A), in which we observed a similar number of infected cells and plaques,
369 respectively. Next, we tested whether the MA104-GCaMP6s-IP_3R-TKO cells efficiently
370 supported rotavirus replication. We compared single-cycle virus yield between parental MA104-
371 GCaMP6s and MA104-GCaMP6s-IP_3R-TKO cells. Cells were infected with MOI 0.01 and
372 maintained in the absence of trypsin to limit the infection to a single round. We found that yields
373 were similar between parental MA104-GCaMP6s and MA104-GCaMP6s-IP_3R-TKO cells,
374 though there was a small increase in rotavirus yield in MA104-GCaMP6s-IP_3R-TKO cells (Figure
375 4C). Thus, the small plaque phenotype on the MA104-GCaMP6s-IP_3R-TKO cells cannot be
376 explained by an inability of these cells to support rotavirus replication. We evaluated rotavirus
377 protein expression by western blot and found similar levels and kinetics of viral protein synthesis
378 for both structural proteins and NSP4 in both cell lines (Figure 4D). Finally, we using
379 immunofluorescence staining of rotavirus-infected cells, we found no difference in viroplasm
380 formation localization of NSP4 to viroplasms (Figure 4E) and this was confirmed by determining
381 no significant difference in the Manders' coefficient for each cell (MA104: 0.047±0.018; MA104-
382 IP_3R-TKO: 0.034±0.013, $p=0.7$). Together, these data indicate the loss of IP_3R did not
383 significantly affect the ability of rotavirus to infect, produce proteins, or assemble new progeny
384 virus during the initial round of replication, and therefore suggests the defect in plaque formation
385 occurs during rotavirus spread through multiple rounds of replication.
386
387 **Role of IP_3R and ICWs in rotavirus spread.**
388 To further investigate why rotavirus did not plaque efficiently on MA104-GCaMP6s-IP_3R-
389 TKO cells, we used fluorescent microscopy to examine the spread of SA11-mRuby in the area
390 around plaques for both parental MA104-GCaMP6s and MA104-GCaMP6s-IP_3R-TKO cells. We

391 performed plaque assays with SA11-mRuby and, on day 4 post-infection, we replaced the
392 overlay with PBS and imaged plaques by brightfield and fluorescence microscopy to visualize
393 mRuby expression in the plaques. In parental MA104 cells, there was full clearing of the plaque
394 and strong mRuby expression in a wide margin around the plaque (Figure 5A, top). In contrast,
395 plaques on MA104-GCaMP6s-IP_3R-TKO cells do not clear and the area of mRuby-positive cells
396 were substantially smaller (Figure 5A, bottom).

397 Next, we examined whether the smaller, turbid plaques formed on MA104-GCaMP6s-
398 IP_3R-TKO cells were the result of a decrease in virus replication kinetics in multi-step replication.
399 We infected parental MA104-GCaMP6s and MA104-GCaMP6s-IP_3R-TKO cells with ~24 PFU
400 (MOI = ~5.9×10^{-5}) to ensure well isolated infected cells, and cultured in the presence of trypsin
401 to visualize SA11-mRuby spread and measure the kinetics of virus replication over 96-hours
402 post-infection. Using live microscopy, we tracked SA11-mRuby spread throughout the
403 monolayer in both parental MA104-GCaMP6s and MA104-GCaMP6s-IP_3R-TKO cells (Figure
404 5B). In parental MA104-GCaMP6s cells, there was more rapid spread with complete destruction
405 of the monolayer by 48-72 hpi (Figure 5B, top). In contrast, virus spread in MA104-GCaMP6s-
406 IP_3R-TKO cells was substantially delayed, especially between 24-48 hpi (Figure 5B, bottom).
407 Next, we determined virus yield from 24-96 hpi and found parental MA104-GCaMP6s cells
408 supported faster virus replication than MA104-GCaMP6s-IP_3R-TKO cells, with peak titers
409 reached in parental cells by 48 hpi (Figure 5C, red line). In contrast, virus replication was
410 significantly lower in MA104-GCaMP6s-IP_3R-TKO cells from 48-72 hpi and did not peak until 72-
411 96 hpi (Figure 5C, blue line).

412 Finally, we examined rotavirus spread using live, time-lapse microscopy to measure the
413 rate of mRuby expression in the absence or presence of trypsin (Figure 5D). As was shown in
414 Figure 3A, in the absence of trypsin there are single infected cells and no spread of mRuby to

415 neighboring cells (data not shown). In the presence of trypsin, rotavirus spread rapidly from the
416 initial infected cells to many of the surrounding cells in parental MA104-GCaMP6s cells, but in
417 MA104-GCaMP6s-IP_3R-TKO cells, this was much slower and primarily to adjacent cells (Figure
418 5D, Movie 5). Together, these data show that in infected cells, the host IP_3R ER Ca^{2+} channel is
419 largely for dispensable rotavirus-induced in Ca^{2+} signaling; however, IP_3R-mediated Ca^{2+}
420 signaling was critical for rotavirus replication and spread.

421

422 **Priming Uninfected Cells via P2Y1-mediated ICWs.**

423 As the loss of IP_3R did not affect rotavirus infectivity or replication in the single cycle
424 replication studies, the above data indicated the defect in rotavirus spread was related to the
425 lack of increased Ca^{2+} signaling in neighboring cells. Increased Ca^{2+} signaling in rotavirus-
426 infected cells has been shown to be critical for robust replication (12, 28, 29), so these
427 observations led us to hypothesize that the increased Ca^{2+} signaling in neighboring uninfected
428 cells could promote rotavirus replication/spread by priming them for infection. Thus, we set out
429 to test this hypothesis by examining how the manipulation of ICWs affected rotavirus spread.

430 We previously showed P2Y1 receptor blockers significantly inhibits rotavirus induced
431 ICWs (17). Thus, we next tested whether blocking ICWs with BPTU, a P2Y1 selective blocker,
432 would also reduce rotavirus spread. We performed a plaque assay using parental MA104 cells
433 in the presence of 1 μM BPTU, or DMSO vehicle control, and found BPTU treatment resulted in
434 significantly smaller plaques (Figure 6). Thus, reducing ICWs by blocking P2Y1 causes a similar
435 reduction in the ability of rotavirus to form plaques as the loss of IP_3R; however, P2Y1 blockers,
436 or even P2Y1 knockout cells, did not fully abrogate ICWs as strongly as MA104-GCaMP6s-IP_3R-
437 TKO cells (17). Therefore, to further test the role of ICWs in rotavirus replication, we examined
438 rotavirus spread in LLC-MK2-GCaMP6s cells, a rhesus monkey kidney cell line we used

439 previously to study Ca^{2+} signaling by Recoviruses (Rhesus enteric caliciviruses) (22). We
440 observed that while rotavirus-infected LLC-MK2-GCaMP6s cells exhibited increased Ca^{2+}
441 signaling, there were no ICWs and therefore no increase in Ca^{2+} signaling in neighboring
442 uninfected cells (Figure 7A). Further, treatment of LLC-MK2-GCaMP6s cells with ADP did not
443 evoke a Ca^{2+} response (Figure 7B, D), indicating a lack of functional P2Y1 signaling. So, we
444 reasoned that if ICWs are a critical factor in rotavirus spread, exogenous expression of P2Y1 in
445 LLC-MK2-GCaMP6s cells might rescue the rotavirus-induced ICW phenotype and increased
446 rotavirus spread. We used lentivirus transduction to generate a stable P2Y1 knock-in LLC-MK2-
447 GCaMP6s cell line (LLC-MK2-GCaMP6s+P2Y1) and presence of an ADP-stimulated Ca^{2+} signal
448 confirmed the P2Y1 was functional in these cells (Figure 7C-D, Movie 6). We confirmed a
449 significant increase in P2Y1 expression in the LLC-MK2-GCaMP6s+P2Y1 cells by qRT-PCR
450 and found that the P2Y1 knock-in did not affect the expression of any other P2Y purinergic
451 receptor (Figure 7E).

452 We next investigated whether exogenous expression of P2Y1 was able to rescue the
453 rotavirus-induced ICWs and, if this affected rotavirus spread. We performed live imaging of
454 rotavirus-infected LLC-MK2-GCaMP6s+P2Y1 cells and found these cells exhibited both higher
455 basal Ca^{2+} signaling and ICWs that originate from rotavirus-infected cells (Figure 8A, Movie 7),
456 resulting in greater Ca^{2+} signaling in the neighboring, uninfected cells than mock-inoculated cells
457 (Figure 8B). Next, we used plaque assays to assess rotavirus spread in LLC-MK2-GCaMP6s
458 cells. In parental LLC-MK2-GCaMP6s cells, rotavirus formed few plaques and those visible were
459 turbid (Figure 8C, top); however, LLC-MK2-GCaMP6s+P2Y1 cells showed more plaques with
460 greater clearing (Figure 8C, bottom). We used fluorescent microscopy to examine spread of
461 SA11-mRuby in the area around plaques for both cell lines. We saw strong mRuby expression
462 for both cell types, but LLC-MK2-GCaMP6s+P2Y1 had significantly more infected cells

463 surrounding the plaques regions with cell monolayer clearing (Figure 8D-E). Thus, introducing
464 P2Y1 expression in LLC-MK2-GCaMP6s cells provides a gain-of-function to produce ICWs in
465 response to rotavirus-infection and this results in better plaque formation and more efficient virus
466 spread. Together these data support our model that the Ca^{2+} signals from P2Y1-mediated ICWs,
467 which requires ER Ca^{2+} release by IP_3R, and primes neighboring cells to promote more robust
468 rotavirus replication and spread *in vitro*.

469 **Discussion.**

470 A hallmark of rotavirus infection, and several other viruses, is an elevation in cytosolic
471 Ca^{2+} and decrease in ER Ca^{2+} stores, which facilitates virus replication and contributes to
472 pathogenesis through a variety of downstream pathways. Host cells also rely on Ca^{2+} signaling
473 pathways to maintain homeostasis. The IP_3R Ca^{2+} channel is an important Ca^{2+} signaling relay
474 hub converting extracellular signals (e.g., ADP) into intracellular signals in which Ca^{2+} itself is
475 the second messenger that controls a myriad of cellular pathways via Ca^{2+}-regulated proteins
476 (30). While the NSP4 viroporin initiates the dysregulation of Ca^{2+} homeostasis during rotavirus
477 infection, the role of IP_3R in generating rotavirus-induced Ca^{2+} signals, particularly in virus-
478 infected cells, had not been characterized. By developing a MA104-GCaMP6s-IP_3R-TKO cell
479 line, we uncovered the following: (i) IP_3R is not required for elevated Ca^{2+} signaling observed in
480 rotavirus-infected cells; (ii) IP_3R ER Ca^{2+} release is critical for P2Y1-mediated ICWs that
481 increase Ca^{2+} signaling in neighboring, uninfected cells; and (iii) while IP_3R Ca^{2+} signaling is not
482 *necessary* for rotavirus replication, the rotavirus-induced ICWs, which require IP_3R, increase the
483 kinetics of rotavirus replication and spread *in vitro*. Together, these findings indicate that
484 increased Ca^{2+} signals in neighboring cells, caused by ICWs, primes these cells to better support
485 rotavirus replication. This process of 'pre-emptively priming' uninfected cells within a viral niche
486 represents a novel mechanistic paradigm by which viruses exploit intercellular host responses
487 to promote their replication.

488 We recently showed that rotavirus-induced increases in cytosolic Ca^{2+} occur through a
489 massive increase in discrete Ca^{2+} signaling events, and a substantial part of this signaling comes
490 from the release of ER Ca^{2+} (20). By examining IP_3R-null cells (both HEK293 and MA104), we
491 have been able to differentiate two distinct types of Ca^{2+} signals that are induced during rotavirus
492 infection: (1) the intracellular Ca^{2+} signals that occur within rotavirus-infected cells, which were
493 IP_3R-independent, and (2) the multicellular ICWs that propagate from infected to neighboring,

494 uninfected cells, which are IP_3R-dependent. By dissecting out these distinct Ca^{2+} signals, we
495 can gain new mechanistic insights into how these signals support rotavirus replication and
496 spread.

497 The intracellular Ca^{2+} signals are IP_3R-independent as knockout of IP_3R did not reduce
498 the number of Ca^{2+} signals observed. Since NSP4 alone is sufficient to increase Ca^{2+} signaling
499 by release of ER Ca^{2+}, we propose that the Ca^{2+} signals observed in the IP_3R-TKO cells are ER
500 Ca^{2+} release events by the NSP4 viroporin (27, 31); however, some of these Ca^{2+} signals could
501 be Ca^{2+} entry via SOCE channels (e.g., Orai) activated by NSP4-mediated decrease in ER Ca^{2+}
502 levels (28). The elevation in Ca^{2+} signaling, in the absence of IP_3R, was sufficient to support
503 rotavirus replication, though the kinetics of multi-step virus replication was impaired (discussed
504 below). The fact that rotavirus encodes an intrinsic capability to drive this degree of Ca^{2+}
505 dysregulation further highlights the critical role Ca^{2+} signaling by NSP4, and perhaps other
506 viroporins, plays in virus replication (3, 7, 12). This raises the question of what cellular pathways
507 are activated by these intracellular Ca^{2+} signals. NSP4 viroporin Ca^{2+} signals are critical for
508 rotavirus replication by initiating the cellular autophagy pathway via activation of the Ca^{2+}-
509 dependent kinase CaMKKβ (12). Further, these dynamic ER Ca^{2+} signals increase mitochondrial
510 metabolism and suppress the activation of apoptosis, which would also benefit rotavirus
511 replication (20). Yet, unraveling the complexity of virus-induced Ca^{2+} signaling remains a
512 burgeoning field, so we are certainly to discover other Ca^{2+}-regulated pathways involved in virus
513 replication.

514 While IP_3R Ca^{2+} signaling was dispensable for rotavirus replication, MA104-GCaMP6s-
515 IP_3R-TKO cells revealed rotavirus induced ICWs significantly increased rotavirus spread and the
516 rate of virus replication. The importance of this paracrine ADP/P2Y1-generated ICW signaling
517 pathway was further supported by rescue of rotavirus plaque formation and increased spread in

518 LLC-MK2-GCaMP6s cells when rotavirus ICW generation was reconstituted by exogenous
519 P2Y1. Further, because MA104-GCaMP6s-IP_3R-TKO cells still released ADP, we can infer that
520 the loss of IP_3R Ca^{2+} signaling, and not other downstream effects of P2Y1 activation, cause the
521 defect in rotavirus spread. Since MA104-GCaMP6s-IP_3R-TKO cells supported replication similar
522 to parental MA104-GCaMP6s cells, these data indicate that IP_3R increased rotavirus replication
523 and spread via an increase in Ca^{2+} signaling in neighboring, uninfected cells through the P2Y1-
524 mediated ICWs.

525 Based on these data, we propose the rotavirus-induced ICWs activate pro-viral Ca^{2+}-
526 regulated pathways in neighboring cells, ultimately priming these cells for more rapid and/or
527 increased replication. This raises the question of which Ca^{2+}-regulated pathways are activated
528 by ICWs in neighboring cells and how do they increase rotavirus replication. One likely pathway
529 is the activation of autophagy because ICWs, like NSP4-mediated Ca^{2+} signals, are generated
530 by release of ER Ca^{2+} and IP_3R Ca^{2+} release can activate CaMKKβ and AMPK phosphorylation
531 and upregulate autophagy (32-34). In rotavirus-infected cells, early autophagosome membranes
532 are usurped to traffic NSP4 and VP7 out of the ER and form a membrane compartment
533 associated with viroplasms (i.e., virus replication complexes) which is the site of final rotavirus
534 assembly (12). Thus, ICWs could activate the early, biosynthetic stages of the autophagy
535 pathway, making more of these membranes available to be utilized upon rotavirus infection.

536 Rotavirus-induced Ca^{2+} signaling is also associated with a broad dysregulation in the
537 actin cytoskeleton, though this has primarily been studied in infected or NSP4 expressing cells
538 and the potential role for ICWs has not been investigated (35). Nevertheless, ICWs are an
539 important mode of multicellular epithelial signaling that directs cell extrusion from monolayers in
540 response to cell damage (36-38). The resulting IP_3R-mediated ER Ca^{2+} release triggers a global,
541 but transient, actin reorganization process termed Ca^{2+}-mediated Actin Reset (CaAR) (39). The

542 CaAR response can drive significant changes in host gene transcription by releasing
543 transcription factors otherwise sequestered in the cytosol (39), and this may help identify cellular
544 pathways activated by ICWs. Importantly, the CaAR responses studied thus far have come from
545 singular signals/damage events, but during rotavirus infection, neighboring cells are stimulated
546 by hours of ICWs, providing ample time and numbers of signals to drive substantial changes.
547 Thus, it will likely require a detailed, multi-omics approach to identify ICW-response pathways
548 and elucidate which of those support rotavirus spread.

549 In summary, we have uncovered a dichotomous role for IP_3R in the overall Ca^{2+} signaling
550 landscape during rotavirus infection and in rotavirus replication and spread. Within infected cells,
551 rotavirus (presumedly via NSP4) generates sufficient Ca^{2+} signaling to support its replication
552 without IP_3R, making this host channel dispensable. In contrast, rotavirus spread was increased
553 by the presence of ICWs and therefore increased Ca^{2+} signaling in neighboring cells, essentially
554 priming them for future rotavirus infection. This implies that viral take-over of the infection niche
555 goes beyond rotavirus-infected cells to include nearby uninfected cells, which undergo
556 "preemptive reprogramming" by repeated ICWs prior to becoming infected. Further, ICWs
557 triggered by rotavirus infection may be a common host response to many different virus
558 infections, and, if so, this P2Y1-mediated Ca^{2+} signaling pathway would have a broader
559 importance in virus replication and pathogenesis. Finally, purinergic signaling is just one of the
560 myriad of other intercellular signaling molecules/pathways that could be exploited by viruses to
561 prime or otherwise reprogram uninfected cells within the infection niche. Identification of
562 analogous virus-induced intercellular signaling pathways may uncover new mechanisms by
563 which viruses, or other microbes, exploit host responses to benefit their replication and spread.

564

Acknowledgments.

We thank Dr. David I. Yule at University of Rochester Medical School for his expertise and advise in generating and characterizing the MA104-GCaMP6s-IP_3R-TKO cells. This work was supported in part by NIH grants R01DK115507 and R01AI158683 (PI: J. M. Hyser). Trainee support for J.L.P. was provided by NIH grants F31AI169983 (PI: J. L. Perry). Trainee support for F.J.S. was provided by NIH grants F31DK132942 (PI: F. J. Scribano). Trainee support for J.T.G was provided by NIH grants F30DK131828 and Histochemical Society Graduate Medical Trainee and Graduate Student Cornerstone Grant (PI: J.T. Gebert). Trainee support for K.A.E. was provided by NIH grants F32DK130288 and Histochemical Society Postdoctoral Keystone Grant. Lentivirus packaging of the P2Y1 expression construct was supported by the ATC Gene Vector Core at Baylor College of Medicine.

576 **Figure Legends.**

577 **Figure 1.** Time lapse Ca^{2+} imaging of rotavirus (RV) infected MA104-GCaMP6s, HEK293-
578 GCaMP6s, and HEK293-GCaMP6s-IP_3R-TKO cells. **A.** Filmstrip of a RV infected MA104 cell
579 (white outline) showing both intracellular and intercellular Ca^{2+} signals. **B.** Representative Ca^{2+}
580 signaling traces showing the change in normalized GCaMP6s fluorescence over time of Mock
581 (black) and RV-infected (red) cells. Intracellular Ca^{2+} signals (magenta bracket) occurred prior
582 to the onset of ICWs (black arrows = representative ICWs). **C.** Quantitation of Ca^{2+} spikes per
583 cell in mock (grey) or RV-infected (red) cells. ****$p<0.001$ by Mann-Whitney T test. **D.** Filmstrip
584 images of representative HEK293-GCaMP6s and HEK293-GCaMP6s-IP_3R-TKO cells (white
585 outline) showing intracellular Ca^{2+} signals over time. **E.** Representative Ca^{2+} signaling traces
586 from RV infected HEK293-GCaMP6s and HEK293-GCaMP6s-IP_3R-TKO and mock uninfected
587 cells. **F.** Quantitation of Ca^{2+} spikes per cell in mock (grey) or RV-infected (red) HEK293-
588 GCaMP6s and HEK293-GCaMP6s-IP_3R-TKO cells. Statistical analysis by Kruskal-Wallis with
589 Dunn's multiple correction where *$p<0.05$ and ****$p<0.0001$. All data are displayed as mean ±
590 SD. Scale bars are 50 μm.

591

592 **Figure 2.** Development of MA104-IP_3R-TKO GCaMP6s cell line. **A.** Schematic workflow for the
593 generation and validation of the MA104-GCaMP6s-IP_3R-TKO cells. **B.** Maximum change in
594 GCaMP6s fluorescence in MA104-GCaMP6s and MA104-GCaMP6s-IP_3R-TKO clones after
595 agonist screening using ADP and AC55541 (PAR2 agonist). **C.** (Left) MA104-GCaMP6s and
596 MA104-GCaMP6s-IP_3R-TKO cells before and after treatment with ADP. Traces (middle) and
597 quantitation (right) of GCaMP6s fluorescence showing Ca^{2+} responses of parental and IP_3R-KO
598 cells upon ADP addition (arrow). **D.** Agonist treatment studies as in (**C**) but using 0.75 μM
599 AC55541. **E.** MA104-GCaMP6s and MA104-GCaMP6s-IP_3R-TKO cells before and after 1 μM

600 thapsigargin treatment. Ca^{2+} signaling traces and quantitation showing normalized GCaMP6s
601 fluorescence after 1 μM thapsigargin treatment (arrow). **F.** Genomic DNA sequencing of IP_3R1,
602 IP_3R2, and IP_3R3 gRNA sites for MA104-GCaMP6s and MA104-GCaMP6s-IP_3R-TKO cells. All
603 data represented as mean ± SD. Statistical analyses were performed by Mann-Whitney test with
604 *p<0.1, ***p<0.001, ****p<0.0001. Scale bars are 50 μm.

605

606 **Figure 3.** Characterization of MA104-GCaMP6s and MA104-GCaMP6s-IP_3R-TKO cells (IP_3R-
607 TKO) during RV infection. **A.** Filmstrip images of RV infected MA104-GCaMP6s cells (white
608 outline, top row) and MA104-GCaMP6s-IP_3R-TKO cells (white outline, bottom row) overtime. **B.**
609 Four representative Ca^{2+} signaling traces from parental MA104-GCaMP6s or MA104-
610 GCaMP6s-IP_3R-TKO cells graphed as the change in normalized GCaMP6s fluorescence over
611 time from RV infected MA104-GCaMP6s cells (red) and MA104-GCaMP6s-IP_3R-TKO cells (dark
612 red). Mock cell traces are shown in black. **C.** Quantitation of the number of Ca^{2+} spikes per cell
613 in mock (grey), RV-infected and neighboring cells for MA104-GCaMP6s and MA104-GCaMP6s-
614 IP_3R-TKO cells. **D.** Maximum change in normalized GCaMP6s fluorescence after supernatant
615 transfer of RV infected MA104-GCaMP6s (red) and MA104-GCaMP6s-IP_3R-TKO (blue) cells to
616 MA104-GCaMP6s sensor cells treated with 10μM BPTU. All data are shown as the mean ± SD.
617 Statistical analyses where performed using Kruskal-Wallis with Dunn's multiple corrections tests
618 with ***p<0.001 & ****p<0.0001. Scale bars are 50 μm.

619

620 **Figure 4.** Characterization of rotavirus infectivity and replication in MA104-GCaMP6s-IP_3R-TKO
621 cells. **A.** Representative images and diameter quantitation of RV plaques formed on MA104-
622 GCaMP6s or MA104-GCaMP6s-IP_3R-TKO cells. **B.** Quantitation of rotavirus infectivity by FFA
623 on MA104-GCaMP6s (red) or MA104-GCaMP6s-IP_3R-TKO (dark red) cells. **C.** One-step

624 rotavirus yield from MA104-GCaMP6s (red) or MA104-GCaMP6s-IP_3R-TKO (dark red) cells was
625 measured by plaque assay and graphed as plaque forming units (PFU) per cell. **D.** Kinetics of
626 rotavirus protein expression in MA104-GCaMP6s and MA104-GCaMP6s-IP_3R-TKO cells was
627 determined by immunoblot for GAPDH (top), NSP4 (middle), and a rabbit anti-rotavirus (strain
628 Alabama) (bottom). **E.** Immunofluorescence of RV-infected MA104-GCaMP6s and MA104-
629 GCaMP6s-IP_3R-TKO cells to detect NSP4 (blue) and NSP5 (magenta), as a marker of
630 viroplasms. All data are shown as the mean ± SD. Statistical analyses were performed using
631 Mann-Whitney T tests with *$p<0.1$ & ****$p<0.0001$. Scale bars are 20 µm.

632

633 **Figure 5.** Loss of IP_3R reduces rotavirus spread. **A.** Visualization of SA11-mRuby in plaques
634 from MA104-GCaMP6s or MA104-GCaMP6s-IP_3R-TKO cells. Brightfield (left) and SA11-mRuby
635 fluorescence (middle) images are merged on the right. Images were acquired with a Plan Fluor
636 objective (NA 0.30) with 10x10mm stich parameters. Scale bars are 1000 µm **B.** SA11-mRuby
637 spread in MA104-GCaMP6s (red) or MA104-GCaMP6s-IP_3R-TKO (blue) cells. Brightfield and
638 fluorescence (SA11-mRuby) images were acquired at the indicated times post infection using a
639 20x Plan Fluor objective (NA 0.45). **C.** SA11-mRuby yield from 24-96 hpi from MA104-GCaMP6s
640 (red) or MA104-GCaMP6s-IP_3R-TKO cells (blue) was measured by plaque assay and graphed
641 as Log_{10} PFU/mL. **D.** Live imaging of SA11-mRuby (RFP) spread in GCaMP6s-expressing
642 parental MA104-GCaMP6s (top) or MA104-GCaMP6s-IP_3R-TKO cells (bottom) from ~30-45 hpi.
643 All data are shown as the mean ± SD. Scale bars are 50 µm in B & D. **$p<0.01$ by T-test.

644

645 **Figure 6.** Blocking P2Y1-mediated ICWs reduces rotavirus plaque size. **A.** Representative
646 image of RV plaques formed on parental MA104 cell monolayers treated with DMSO (Top) or 1

647 μM BPTU (bottom). **B.** Measurement of plaque diameter for DMSO and 1 μM BPTU treated
648 cells. Data are shown as the mean ± SD. ***p<0.001 by Mann-Whitney T test.

649

650 **Figure 7.** P2Y1 Ca^{2+} signaling in LLC-MK2 cells. **A.** Ca^{2+} spikes per cell in mock (black),
651 rotavirus-infected (blue), and neighboring (NB3) uninfected (light blue) cells. ****p<0.0001 by
652 Kruskal-Wallis with Dunn's multiple corrections. **B.** Representative images of LLC-MK2 cell
653 monolayers before (top) and after (bottom) treatment with 25 nM ADP. **C.** Representative images
654 of LLC-MK2 and LLC-MK2+P2Y1 cell monolayers before (left) or after (right) agonist treatment
655 with 25nM ADP. **D.** Ca^{2+} signaling traces of LLC-MK2 (blue line) and LLC-MK2+P2Y1 cells
656 (purple line) after treatment with 25 nM ADP (arrow). **E.** P2Y purinergic receptor mRNA
657 expression by qPCR in LLC-MK2 and LLC-MK2+P2Y1 cells. Data were normalized to 18s
658 mRNA and plotted relative to P2Y12 mRNA transcript levels. ****p<0.0001 by 1-way ANOVA
659 with Bonferroni's multiple corrections. All data represented as mean ± SD. Scale bars are all 50
660 μm.

661

662 **Figure 8.** Reconstituting ICWs in LLC-MK2+P2Y1 cells increases rotavirus spread. **A.** Filmstrip
663 images of RV ICWs in LLC-MK2+P2Y1 cells. Scale bar is 50 μm. **B.** Ca^{2+} spikes per cell in
664 mock or RV infected and neighboring (NB3) LLC-MK2 cells. ***p<0.001 by Kruskal-Wallis with
665 Dunn's multiple correction test. **C.** Representative images of RV plaques formed on LLC-MK2
666 (Top) and LLC-MK2+P2Y1 (bottom) monolayers. **D.** RV infected (red) LLC-MK2 (left) and LLC-
667 MK2+P2Y1 (right) cell monolayers. White circles designate the margins of RV foci. Images
668 were captured using a Plan Fluor 10x objective (NA 0.30) with 10 x10mm stich parameters. In
669 these stitched images, the scale bar represents 2000 μm. **E.** Quantitation of mean

670 fluorescence intensity of TRITC channel. *$p<0.05$ by Mann-Whitney T-test. All data are shown

671 as the mean ± SD.

672 **Table 1.** African green monkey IP_3R1, IP_3R2, and IP_3R3 gRNA sequences and exon target
673 sites.

Gene	Species	gRNA sequence (5')	gRNA target
IP_3R1	*Chlorocebus pygerythrus*	GCTGGATGACATCGTTCGCGTGG	exon 33
IP_3R2	*Chlorocebus pygerythrus*	CCACATGCACGTTGACCGGGATC	exon 19
IP_3R3	*Chlorocebus pygerythrus*	GTGCCCCATGAACCGCTACTCGG	exon 3

674

675 **Table 2.** African green monkey IP_3R1, IP_3R2, and IP_3R3 sequencing primers.

Gene	Species	Forward Sequence (5')	Reverse Sequence (5')
IP_3R1	*Chlorocebus pygerythrus*	TTTTTAGGGCCCGTGTGGTA	TTCATTCAGGTCGCATCCCC
IP_3R2	*Chlorocebus pygerythrus*	GAACTGAATGGGGCGAAACCT	TCTTCAACAAATTCCATTGTCAGG
IP_3R3	*Chlorocebus pygerythrus*	TCCAACTCCTGCCTCCTTTG	CACTGTCTCCACAAGCCACT

676

677 Table 3. Quantitative PCR primer sequences

Gene	Forward 5' Sequence	Reverse 5' Sequence
18s	GATATGCTCATGTGGTGTTG	AATCTTCTTCAGTCGCTCCA
P2Y1	CGTGCTGGTGTGGCTCATT	GGACCCCGGTACCTGAGTAGA
P2Y2	GAACTGACATGCAGAGGATAGAAGAT	GCCGGCGTGGACTCTGT
P2Y4	CCGTCCTGTGCCATGACA	TGACCGCCGAGCTGAAGT
P2Y6	GCCGGCGACCACATGA	GACCCTGCCTCTGCCATTT
P2Y11	CTGGAGCGCTTCCTCTTCAC	GGTAGCGGTTGAGGCTGATG
P2Y12	AGGTCCTCTTCCCACTGCTCTA	CATCGCCAGGCCATTTGT
P2Y14	TTCCTTTCAAGATCCTTGGTGACT	GCAGAGACCCTGCACACAAA

678

679

680 REFERENCES CITED

681

682 1. Berridge MJ. 2012. Calcium signalling remodelling and disease. Biochem Soc Trans 40:297-
683 309.
684 2. Zhou Y, Frey TK, Yang JJ. 2009. Viral calciomics: interplays between Ca2+ and virus. Cell
685 Calcium 46:1-17.
686 3. Hyser JM, Estes MK. 2015. Pathophysiological Consequences of Calcium-Conducting
687 Viroporins. Annu Rev Virol 2:473-96.
688 4. Michelangeli F, Ruiz MC, del Castillo JR, Ludert JE, Liprandi F. 1991. Effect of rotavirus
689 infection on intracellular calcium homeostasis in cultured cells. Virology 181:520-7.
690 5. Tian P, Estes MK, Hu Y, Ball JM, Zeng CQ, Schilling WP. 1995. The rotavirus nonstructural
691 glycoprotein NSP4 mobilizes Ca2+ from the endoplasmic reticulum. J Virol 69:5763-72.
692 6. Berkova Z, Morris AP, Estes MK. 2003. Cytoplasmic calcium measurement in rotavirus
693 enterotoxin-enhanced green fluorescent protein (NSP4-EGFP) expressing cells loaded with
694 Fura-2. Cell Calcium 34:55-68.
695 7. Zambrano JL, Diaz Y, Pena F, Vizzi E, Ruiz MC, Michelangeli F, Liprandi F, Ludert JE. 2008.
696 Silencing of rotavirus NSP4 or VP7 expression reduces alterations in Ca2+ homeostasis
697 induced by infection of cultured cells. J Virol 82:5815-24.
698 8. Ericson BL, Graham DY, Mason BB, Estes MK. 1982. Identification, synthesis, and
699 modifications of simian rotavirus SA11 polypeptides in infected cells. J Virol 42:825-39.
700 9. Sastri NP, Crawford SE, Estes MK. 2016. Pleiotropic Properties of Rotavirus Nonstructrual
701 Protein 4 (NSP4) and their Effects on Viral Replication and Pathogenesis, p 145-174. *In*
702 Svensson L, Desselberger U, Greenberg HB, Estes MK (ed), Viral Gastroenteritis: Molecular
703 Epidemiology and Pathogenesis. Elsevier Academic Press, Amsterdam.
704 10. Hyser JM, Collinson-Pautz MR, Utama B, Estes MK. 2010. Rotavirus disrupts calcium
705 homeostasis by NSP4 viroporin activity. mBio 1:e00265-10.
706 11. Pham T, Perry JL, Dosey TL, Delcour AH, Hyser JM. 2017. The Rotavirus NSP4 Viroporin
707 Domain is a Calcium-conducting Ion Channel. Sci Rep 7:43487.
708 12. Crawford SE, Hyser JM, Utama B, Estes MK. 2012. Autophagy hijacked through viroporin-
709 activated calcium/calmodulin-dependent kinase kinase-beta signaling is required for rotavirus
710 replication. Proc Natl Acad Sci U S A 109:E3405-E3413.
711 13. Crawford SE, Criglar JM, Liu Z, Broughman JR, Estes MK. 2019. COPII Vesicle Transport Is
712 Required for Rotavirus NSP4 Interaction with the Autophagy Protein LC3 II and Trafficking to
713 Viroplasms. J Virol 94.
714 14. Foskett JK, White C, Cheung KH, Mak DO. 2007. Inositol trisphosphate receptor Ca2+ release
715 channels. Physiol Rev 87:593-658.
716 15. Lock JT, Alzayady KJ, Yule DI, Parker I. 2018. All three IP3 receptor isoforms generate Ca(2+)
717 puffs that display similar characteristics. Sci Signal 11.
718 16. Foskett JK, Daniel Mak DO. 2010. Regulation of IP(3)R Channel Gating by Ca(2+) and Ca(2+)
719 Binding Proteins. Curr Top Membr 66:235-72.
720 17. Chang-Graham AL, Perry JL, Engevik MA, Engevik KA, Scribano FJ, Gebert JT, Danhof HA,
721 Nelson JC, Kellen JS, Strtak AC, Sastri NP, Estes MK, Britton RA, Versalovic J, Hyser JM.
722 2020. Rotavirus induces intercellular calcium waves through ADP signaling. Science 370.
723 18. Ando H, Hirose M, Mikoshiba K. 2018. Aberrant IP(3) receptor activities revealed by
724 comprehensive analysis of pathological mutations causing spinocerebellar ataxia 29. Proc Natl
725 Acad Sci U S A 115:12259-12264.
726 19. Lung O, Candlish R, Nebroski M, Kruckiewicz P, Buchanan C, Moniwa M. 2021. High-
727 throughput sequencing for species authentication and contamination detection of 63 cell lines.
728 Sci Rep 11:21657.
729 20. Chang-Graham AL, Perry JL, Strtak AC, Ramachandran NK, Criglar JM, Philip AA, Patton JT,
730 Estes MK, Hyser JM. 2019. Rotavirus Calcium Dysregulation Manifests as Dynamic Calcium
731 Signaling in the Cytoplasm and Endoplasmic Reticulum. Sci Rep 9:10822.

732 21. Perry JL, Ramachandran NK, Utama B, Hyser JM. 2015. Use of genetically-encoded calcium
733 indicators for live cell calcium imaging and localization in virus-infected cells. Methods 90:28-38.
734 22. Strtak AC, Perry JL, Sharp MN, Chang-Graham AL, Farkas T, Hyser JM. 2019. Recovirus NS1-
735 2 Has Viroporin Activity That Induces Aberrant Cellular Calcium Signaling To Facilitate Virus
736 Replication. mSphere 4.
737 23. Philip AA, Dai J, Katen SP, Patton JT. 2020. Simplified Reverse Genetics Method to Recover
738 Recombinant Rotaviruses Expressing Reporter Proteins. J Vis Exp doi:10.3791/61039.
739 24. Hyser JM, Zeng CQ, Beharry Z, Palzkill T, Estes MK. 2008. Epitope mapping and use of
740 epitope-specific antisera to characterize the VP5* binding site in rotavirus SA11 NSP4. Virology
741 373:211-228.
742 25. Criglar JM, Hu L, Crawford SE, Hyser JM, Broughman JR, Prasad BV, Estes MK. 2014. A novel
743 form of rotavirus NSP2 and phosphorylation-dependent NSP2-NSP5 interactions are associated
744 with viroplasm assembly. J Virol 88:786-98.
745 26. Maynard JP, Lee JS, Sohn BH, Yu X, Lopez-Terrada D, Finegold MJ, Goss JA, Thevananther
746 S. 2015. P2X3 purinergic receptor overexpression is associated with poor recurrence-free
747 survival in hepatocellular carcinoma patients. Oncotarget 6:41162-79.
748 27. Michelangeli F, Liprandi F, Chemello ME, Ciarlet M, Ruiz MC. 1995. Selective depletion of
749 stored calcium by thapsigargin blocks rotavirus maturation but not the cytopathic effect. J Virol
750 69:3838-3847.
751 28. Hyser JM, Utama B, Crawford SE, Broughman JR, Estes MK. 2013. Activation of the
752 endoplasmic reticulum calcium sensor STIM1 and store-operated calcium entry by rotavirus
753 requires NSP4 viroporin activity. J Virol 87:13579-88.
754 29. Ruiz MC, Cohen J, Michelangeli F. 2000. Role of Ca2+in the replication and pathogenesis of
755 rotavirus and other viral infections. Cell Calcium 28:137-49.
756 30. Berridge MJ, Lipp P, Bootman MD. 2000. The versatility and universality of calcium signalling.
757 Nat Rev Mol Cell Biol 1:11-21.
758 31. Ruiz MC, Aristimuno OC, Diaz Y, Pena F, Chemello ME, Rojas H, Ludert JE, Michelangeli F.
759 2007. Intracellular disassembly of infectious rotavirus particles by depletion of Ca2+
760 sequestered in the endoplasmic reticulum at the end of virus cycle. Virus Res 130:140-150.
761 32. Kania E, Roest G, Vervliet T, Parys JB, Bultynck G. 2017. IP(3) Receptor-Mediated Calcium
762 Signaling and Its Role in Autophagy in Cancer. Front Oncol 7:140.
763 33. Parys JB, Decuypere JP, Bultynck G. 2012. Role of the inositol 1,4,5-trisphosphate
764 receptor/Ca2+-release channel in autophagy. Cell Commun Signal 10:17.
765 34. Megha, Hasan G. 2017. Control of protein translation by IP(3)R-mediated Ca(2+) release in
766 Drosophila neuroendocrine cells. Fly (Austin) 11:0.
767 35. Zambrano JL, Sorondo O, Alcala A, Vizzi E, Diaz Y, Ruiz MC, Michelangeli F, Liprandi F, Ludert
768 JE. 2012. Rotavirus infection of cells in culture induces activation of RhoA and changes in the
769 actin and tubulin cytoskeleton. PLoS One 7:e47612.
770 36. Mitchell SJ, Rosenblatt J. 2021. Early mechanical selection of cell extrusion and extrusion
771 signaling in cancer. Curr Opin Cell Biol 72:36-40.
772 37. Rosenblatt J, Raff MC, Cramer LP. 2001. An epithelial cell destined for apoptosis signals its
773 neighbors to extrude it by an actin- and myosin-dependent mechanism. Curr Biol 11:1847-57.
774 38. Takeuchi Y, Narumi R, Akiyama R, Vitiello E, Shirai T, Tanimura N, Kuromiya K, Ishikawa S,
775 Kajita M, Tada M, Haraoka Y, Akieda Y, Ishitani T, Fujioka Y, Ohba Y, Yamada S, Hosokawa Y,
776 Toyama Y, Matsui T, Fujita Y. 2020. Calcium Wave Promotes Cell Extrusion. Curr Biol 30:670-
777 681 e6.
778 39. Wales P, Schuberth CE, Aufschnaiter R, Fels J, Garcia-Aguilar I, Janning A, Dlugos CP,
779 Schafer-Herte M, Klingner C, Walte M, Kuhlmann J, Menis E, Hockaday Kang L, Maier KC, Hou
780 W, Russo A, Higgs HN, Pavenstadt H, Vogl T, Roth J, Qualmann B, Kessels MM, Martin DE,
781 Mulder B, Wedlich-Soldner R. 2016. Calcium-mediated actin reset (CaAR) mediates acute cell
782 adaptations. Elife 5.

783

Figure 1

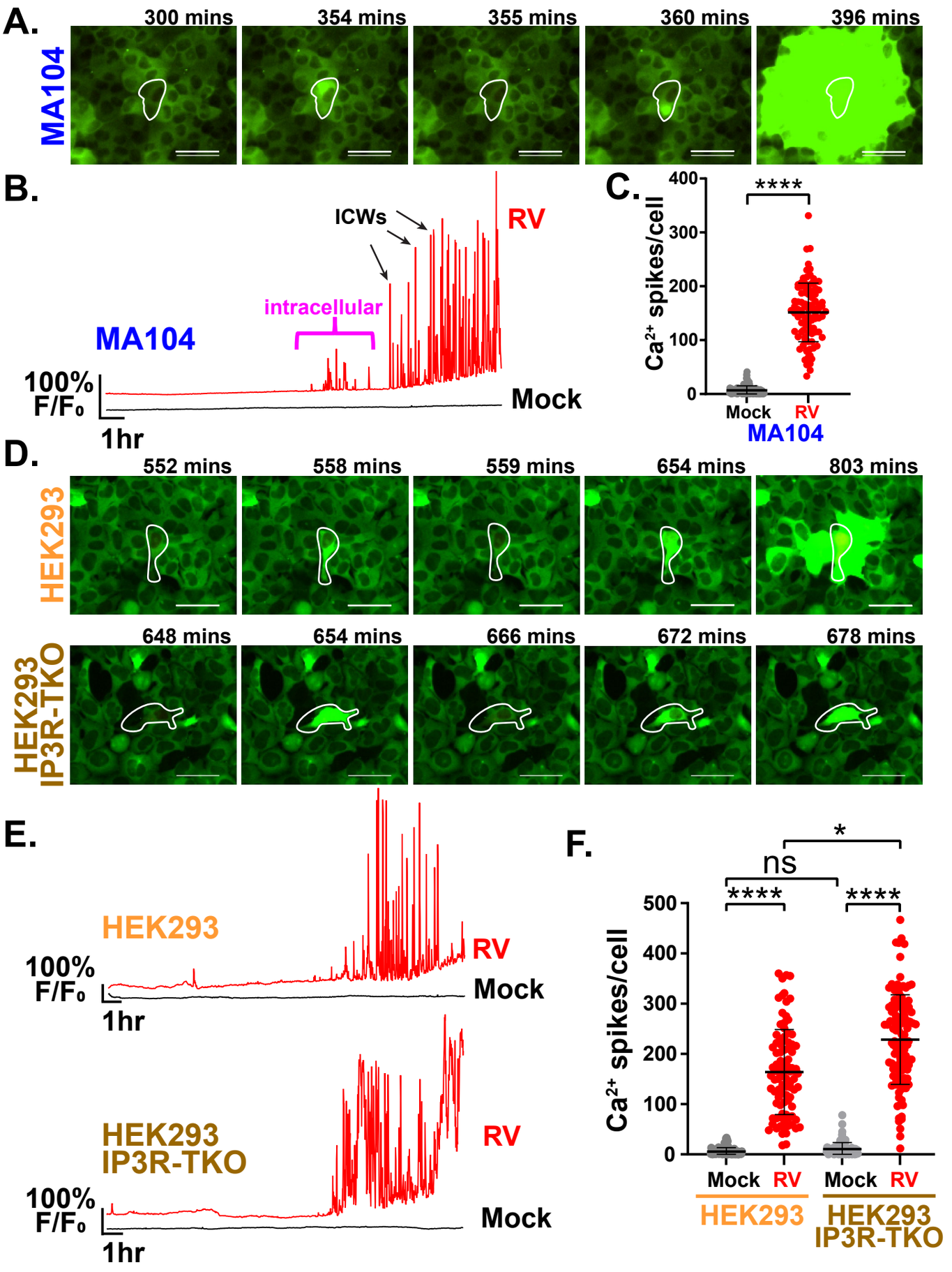

Figure 1. Time lapse Ca2+ imaging of rotavirus (RV) infected MA104-GCaMP6s, HEK293-GCaMP6s, and HEK-293-GCaMP6s-IP3R-TKO cells. A. Filmstrip of a RV infected MA104 cell (white outline) showing both intracellular and intercellular Ca2+ signals. B. Representative Ca2+ signaling traces showing the change in normalized GCaMP6s fluorescence over time of Mock (black) and RV-infected (red) cells. Intracellular Ca2+ signals (magenta bracket) occurred prior to the onset of ICWs (black arrows = representative ICWs). C. Quantitation of Ca2+ spikes per cell in mock (grey) or RV-infected (red) cells. ****p<0.001 by Mann-Whitney T test. D. Filmstrip images of representative HEK293-GCaMP6s and HEK293-GCaMP6s-IP3R-TKO cells (white outline) showing intracellular Ca2+ signals over time. E. Representative Ca2+ signaling traces from RV infected HEK293-GCaMP6s and HEK293-GCaMP6s-IP3R-TKO and mock uninfected cells. F. Quantitation of Ca2+ spikes per cell in mock (grey) or RV-infected (red) HEK-293-GCaMP6s and HEK293-GCaMP6s-IP3R-TKO cells. Statistical analysis by Kruskal-Wallis with Dunn's multiple correction where *p<0.05 and ****p<0.0001. All data are displayed as mean ± SD. Scale bars are 50 µm.

Figure 2

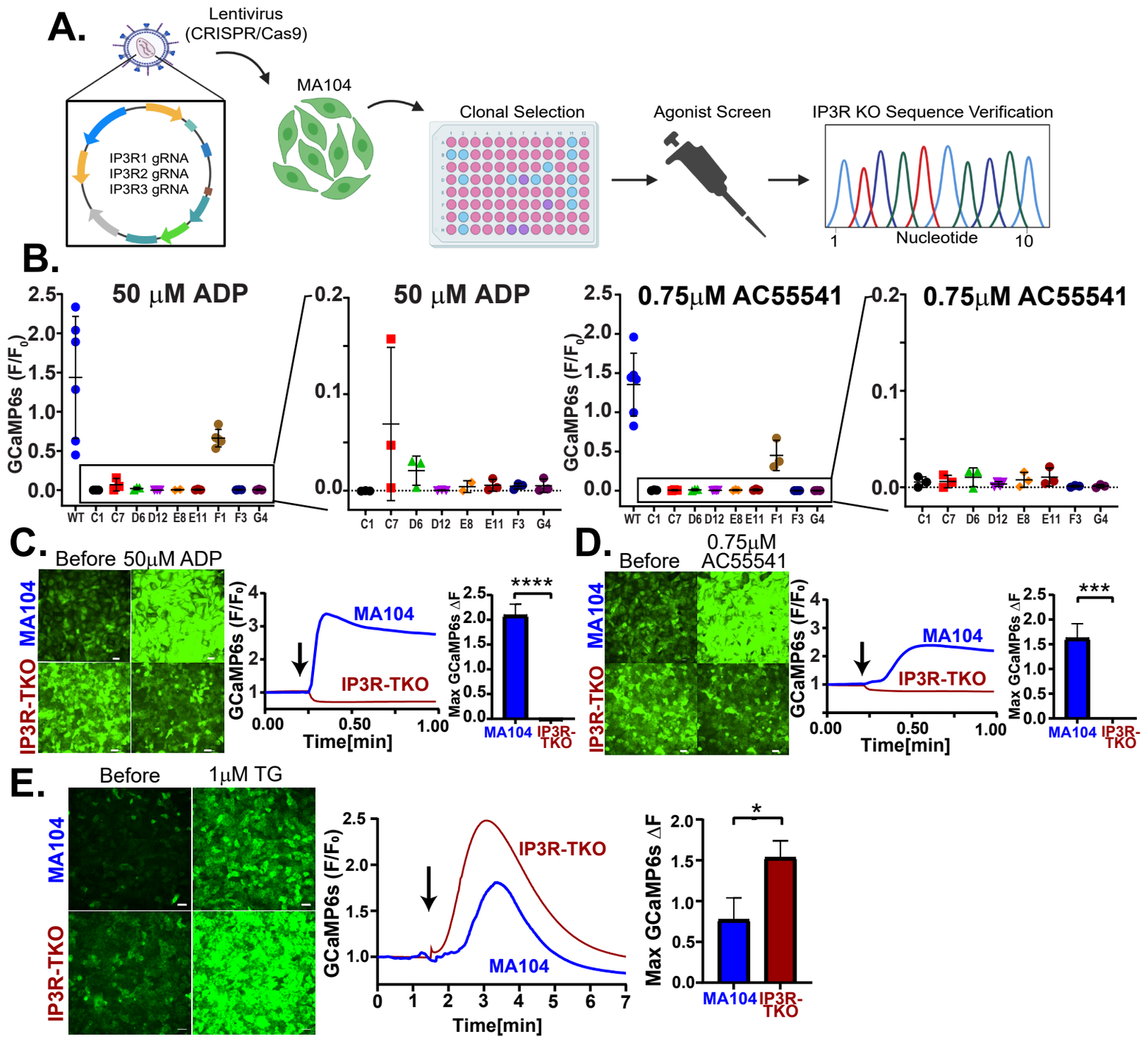

F.

IP3R1

WT: CTTCCGCTGGATGACATCGTTCGCGTGGTGACCCAT

cl.F3: CTTCCGC----------GTGGTGACCCAT 6/6

IP3R2

WT: ATGCTCCACATGCACGTTGACCGGGATCCCCAGGAG

cl.F3: ATGCTCCACGTTGACCGTTGACCGGGATCCCCAGGAG 1/6

cl.F3: A----------CGTTGACCGGGATCCCCAGGAG 1/6

cl.F3: ----------325bp deletion ---------- 4/6

IP3R3

WT: AAGGTGTGCCCCATGAACCGCTACTCGGCCCAGAAG

cl.F3: AAGGTGTGCCCCATGAACCGCTTACTCGGCCCAGAAG 6/6

Figure 2. Development of MA104-IP3R-TKO GCaMP6s cell line. A. Schematic workflow for the generation and validation of the MA104-GCaMP6s-IP3R-TKO cells. B. Maximum change in GCaMP6s fluorescence in MA104-GCaMP6s and MA104-GCaMP6s-IP3R-TKO clones after agonist screening using ADP and AC55541 (PAR2 agonist). C. (Left) MA104-GCaMP6s and MA104-GCaMP6s-IP3R-TKO cells before and after treatment with ADP. Traces (middle) and quantitation (right) of GCaMP6s fluorescence showing Ca2+ responses of parental and IP3R-KO cells upon ADP addition (arrow). D. Agonist treatment studies as in (C) but using 0.75 μM AC55541. E. MA104-GCaMP6s and MA104-GCaMP6s-IP3R-TKO cells before and after 1 μM thapsigargin treatment. Ca2+ signaling traces and quantitation showing normalized GCaMP6s fluorescence after 1 μM thapsigargin treatment (arrow). F. Genomic DNA sequencing of IP3R1, IP3R2, and IP3R3 gRNA sites for MA104-GCaMP6s and MA104-GCaMP6s-IP3R-TKO cells. All data represented as mean ± SD. Statistical analyses were performed by Mann-Whitney test with *p<0.1, ***p<0.001, ****p<0.0001. Scale bars are 50 μm.

Figure 3

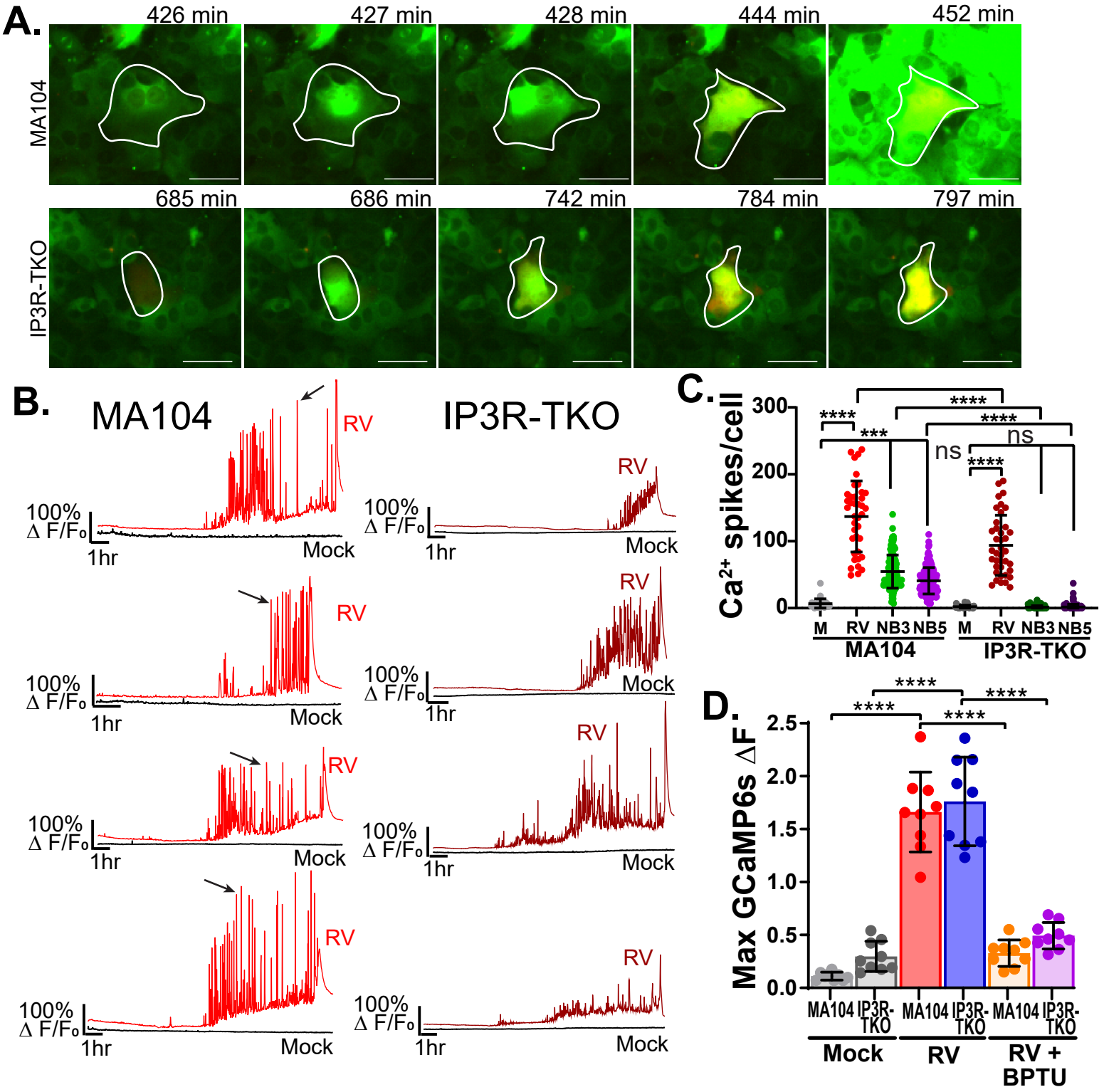

Figure 3. Characterization of MA104-GCaMP6s and MA104-GCaMP6s-IP3R-TKO cells (IP3R-TKO) during RV infection. A. Filmstrip images of RV infected MA104-GCaMP6s cells (white outline, top row) and MA104-GCaMP6s-IP3R-TKO cells (white outline, bottom row) overtime. B. Four representative Ca2+ signaling traces from parental MA104-GCaMP6s or MA104-GCaMP6s-IP3R-TKO cells graphed as the change in normalized GCaMP6s fluorescence over time from RV infected MA104-GCaMP6s cells (red) and MA104-GCaMP6s-IP3R-TKO cells (dark red). Mock cell traces are shown in black. C. Quantitation of the number of Ca2+ spikes per cell in mock (grey), RV-infected and neighboring cells for MA104-GCaMP6s and MA104-GCaMP6s-IP3R-TKO cells. D. Maximum change in normalized GCaMP6s fluorescence after supernatant transfer of RV infected MA104-GCaMP6s (red) and MA104-GCaMP6s-IP3R-TKO (blue) cells to MA104-GCaMP6s sensor cells treated with 10μM BPTU. All data are shown as the mean ± SD. Statistical analyses where performed using Kruskal-Wallis with Dunn's multiple corrections tests with ***p<0.001 & ****p<0.0001. Scale bars are 50 μm.

Figure 4

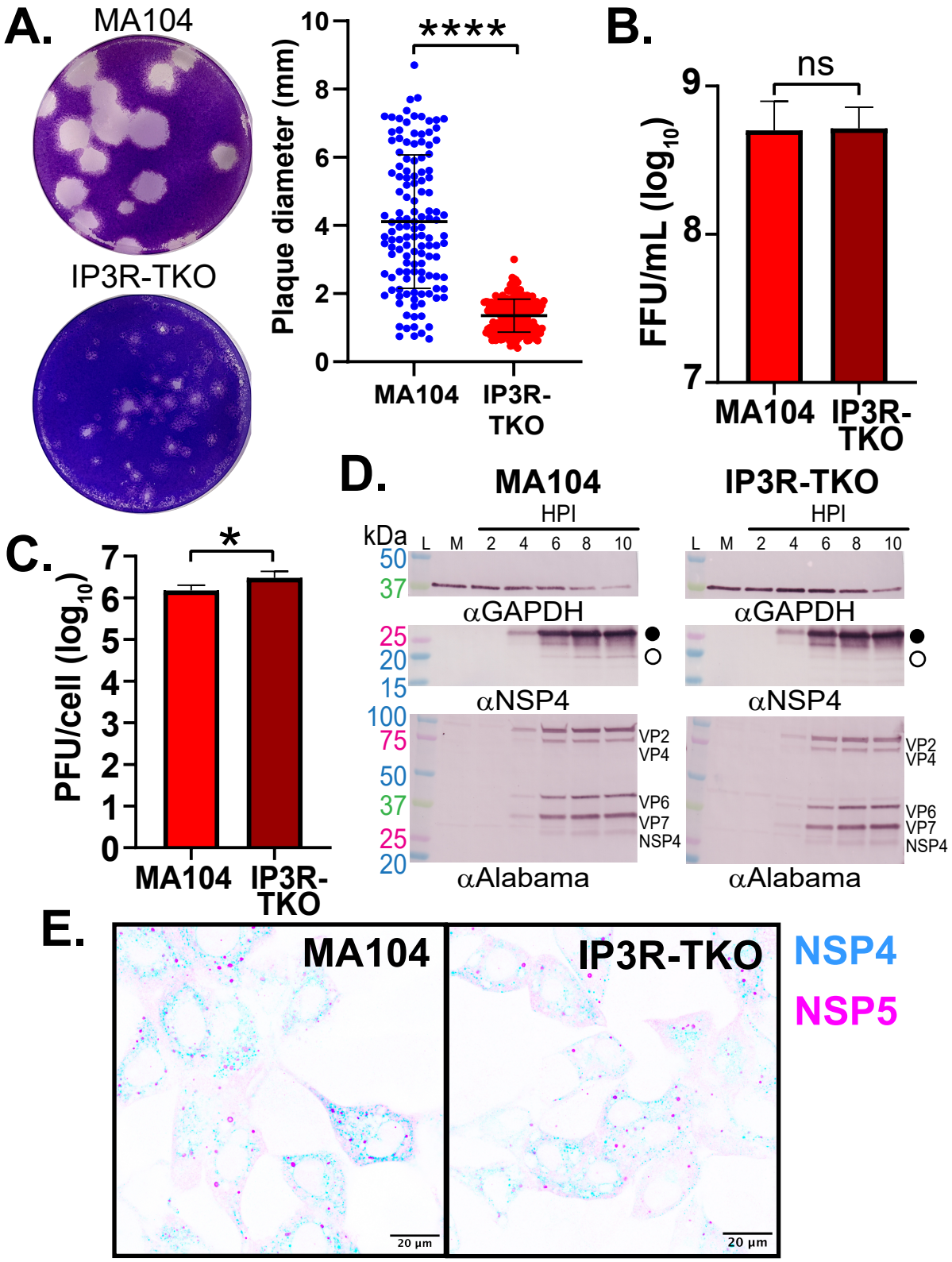

Figure 4. Characterization of rotavirus infectivity and replication in MA104-GCaMP6s-IP3R-TKO cells. A. Representative images and diameter quantitation of RV plaques formed on MA104-GCaMP6s or MA104-GCaMP6s-IP-3R-TKO cells. B. Quantitation of rotavirus infectivity by FFA on MA104-GCaMP6s (red) or MA104-GCaMP6s-IP-3R-TKO (dark red) cells. C. One-step rotavirus yield from MA104-GCaMP6s (red) or MA104-GCaMP6s-IP3R-TKO (dark red) cells was measured by plaque assay and graphed as plaque forming units (PFU) per cell. D. Kinetics of rotavirus protein expression in MA104-GCaMP6s and MA104-GCaMP6s-IP3R-TKO cells was determined by immunoblot for GAPDH (top), NSP4 (middle), and a rabbit anti-rotavirus (strain Alabama) (bottom). E. Immunofluorescence of RV-infected MA104-GCaMP6s and MA104-GCaMP6s-IP3R-TKO cells to detect NSP4 (blue) and NSP5 (magenta), as a marker of viroplasms. All data are shown as the mean ± SD. Statistical analyses were performed using Mann-Whitney T tests with *p<0.1 & ****p<0.0001. Scale bars are 20 µm.

Figure 5

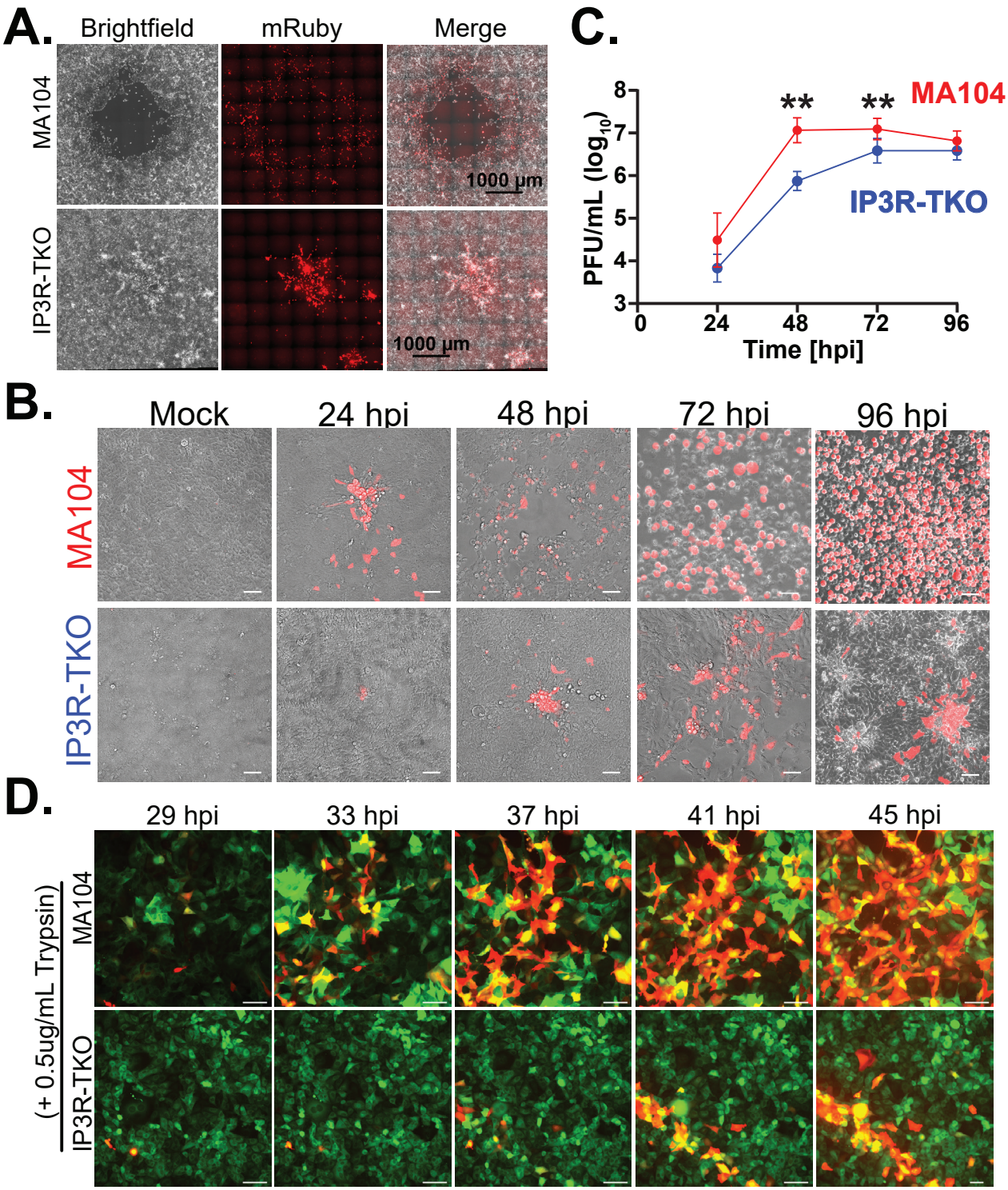

Figure 5. Loss of IP3R reduces rotavirus spread. A. Visualization of SA11-mRuby in plaques from MA104-GCaMP6s or MA104-GCaMP6s-IP3R-TKO cells. Brightfield (left) and SA11-mRuby fluorescence (middle) images are merged on the right. Images were acquired with a Plan Fluor objective (NA 0.30) with 10x10mm stich parameters. Scale bars are 1000 µm B. SA11-mRuby spread in MA104-GCaMP6s (red) or MA104-GCaMP6s-IP3R-TKO (blue) cells. Brightfield and fluorescence (SA11-mRuby) images were acquired at the indicated times post infection using a 20x Plan Fluor objective (NA 0.45). C. SA11-mRuby yield from 24-96 hpi from MA104-GCaMP6s (red) or MA104-GCaMP6s-IP3R-TKO cells (blue) was measured by plaque assay and graphed as Log10 PFU/mL. D. Live imaging of SA11-mRuby (RFP) spread in GCaMP6s-expressing parental MA104-GCaMP6s (top) or MA104-GCaMP6s-IP3R-TKO cells (bottom) from ~30-45 hpi. All data are shown as the mean ± SD. Scale bars are 50 µm in B & D. **$p<0.01$ by T-test.

Figure 6

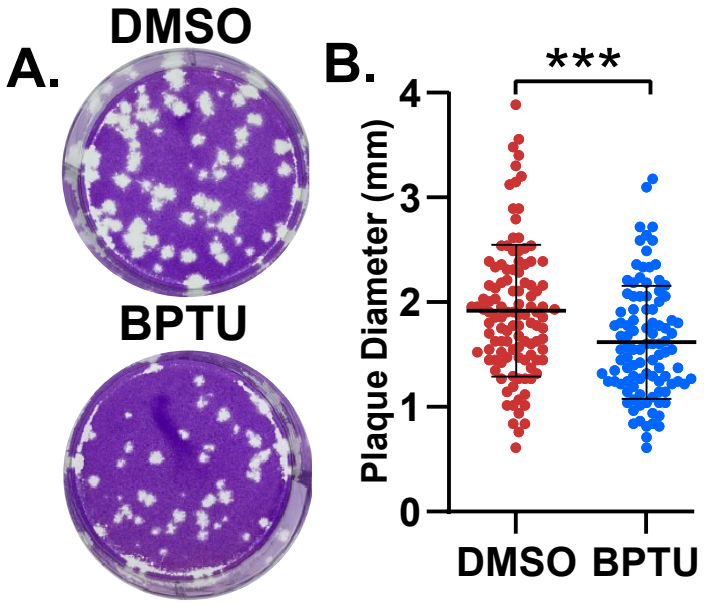

Figure 6. Blocking P2Y1-mediated ICWs reduces rotavirus plaque size. A. Representative image of RV plaques formed on parental MA104 cell monolayers treated with DMSO (Top) or 1 μM BPTU (bottom). B. Measurement of plaque diameter for DMSO and 1 μM BPTU treated cells. Data are shown as the mean ± SD. ***$p<0.001$ by Mann-Whitney T test.

Figure 7

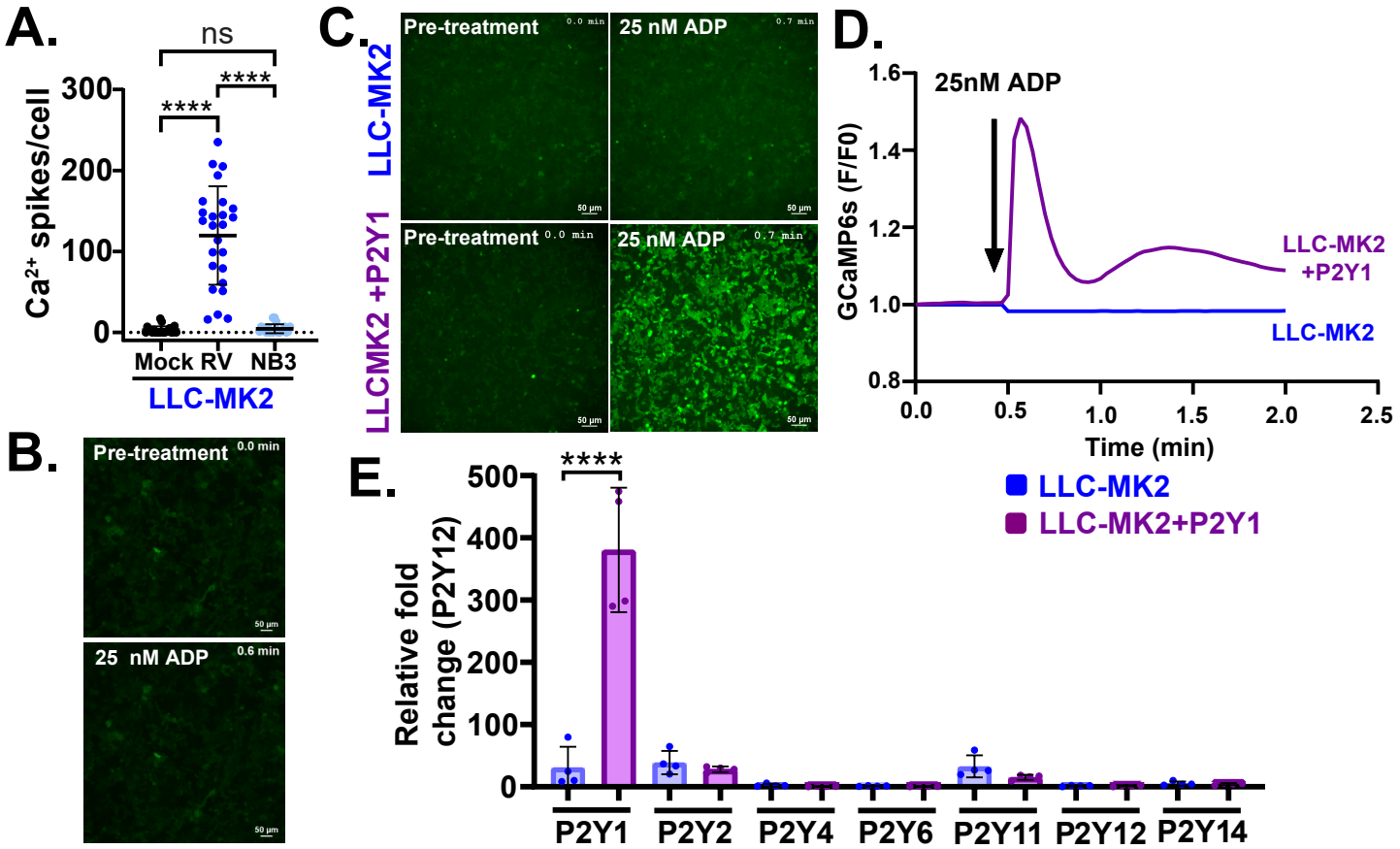

Figure 7. P2Y1 Ca2+ signaling in LLC-MK2 cells. A. Ca2+ spikes per cell in mock (black), rotavirus-infected (blue), and neighboring (NB3) uninfected (light blue) cells. ****p<0.0001 by Kruskal-Wallis with Dunn's multiple corrections. B. Representative images of LLC-MK2 cell monolayers before (top) and after (bottom) treatment with 25 nM ADP. C. Representative images of LLC-MK2 and LLC-MK2+P2Y1 cell monolayers before (left) or after (right) agonist treatment with 25nM ADP. D. Ca2+ signaling traces of LLC-MK2 (blue line) and LLC-MK2+P2Y1 cells (purple line) after treatment with 25 nM ADP (arrow). E. P2Y purinergic receptor mRNA expression by qPCR in LLC-MK2 and LLC-MK2+P2Y1 cells. Data were normalized to 18s mRNA and plotted relative to P2Y12 mRNA transcript levels. ****p<0.0001 by 1-way ANOVA with Bonferroni's multiple corrections. All data represented as mean ± SD. Scale bars are all 50 µm.

Figure 8

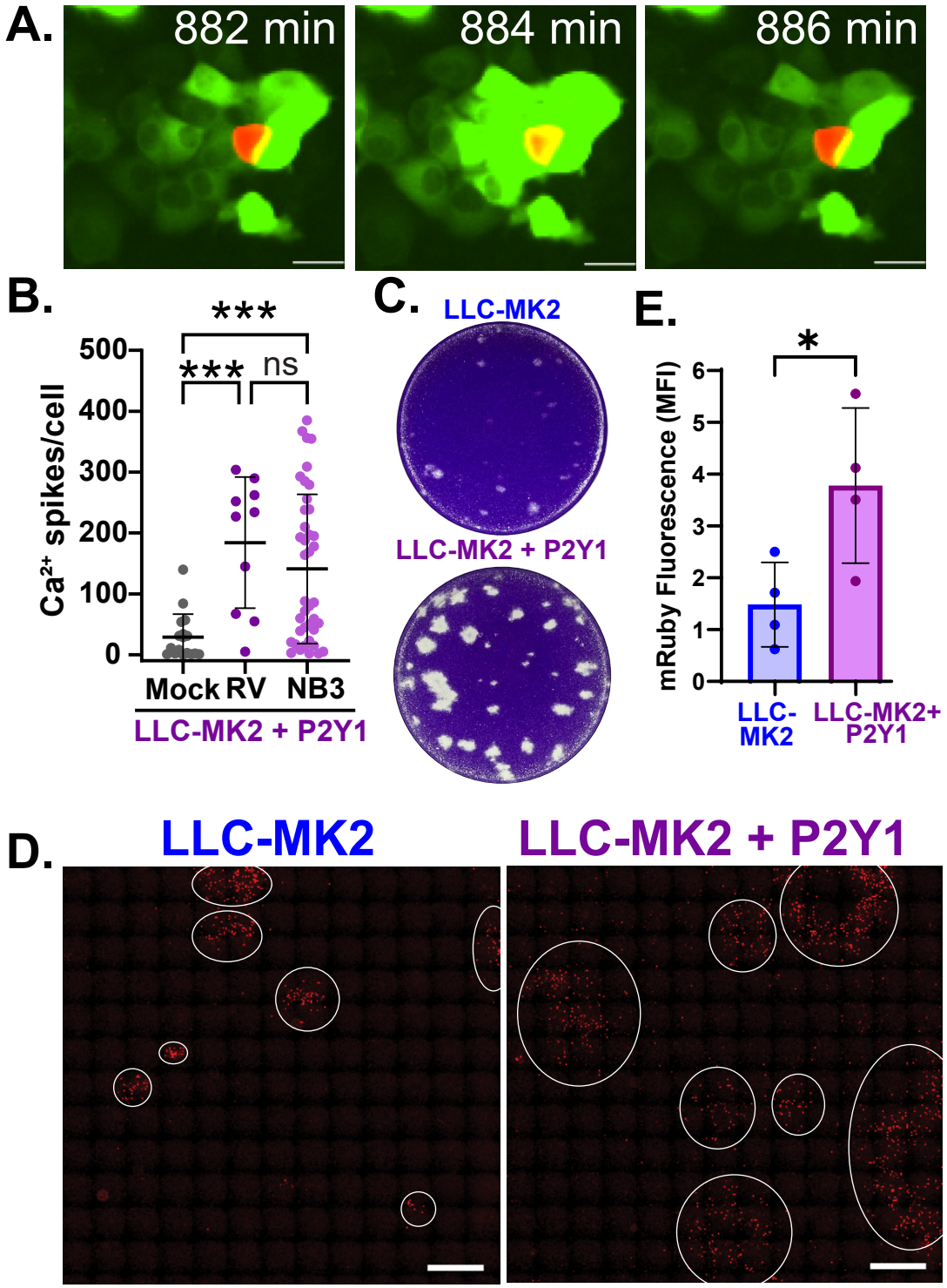

Figure 8. Reconstituting ICWs in LLC-MK2+P2Y1 cells increases rotavirus spread. A. Filmstrip images of RV ICWs in LLC-MK2+P2Y1 cells. Scale bar is 50 µm. B. Ca2+ spikes per cell in mock or RV infected and neighboring (NB3) LLC-MK2 cells. ***$p<0.001$ by Kruskal-Wallis with Dunn's multiple correction test. C. Representative images of RV plaques formed on LLC-MK2 (Top) and LLC-MK2+P2Y1 (bottom) monolayers. D. RV infected (red) LLC-MK2 (left) and LLC-MK2+P2Y1 (right) cell monolayers. White circles designate the margins of RV foci. Images were captured using a Plan Fluor 10x objective (NA 0.30) with 10 x10mm stich parameters. In these stitched images, the scale bar represents 2000 µm. E. Quantitation of mean fluorescence intensity of TRITC channel. *$p<0.05$ by Mann-Whitney T-test. All data are shown as the mean ± SD.